PHYSICAL REVIEW D **91,** 114506 (2015)

Y-stringlike behavior of a static baryon at finite temperature

Ahmed S. Bakry,[1,*] Xurong Chen,[1] and Peng-Ming Zhang[1,2]
[1]*Institute of Modern Physics, Chinese Academy of Sciences, Lanzhou 730000, China*
[2]*State Key Laboratory of Theoretical Physics, Institute of Theoretical Physics,*
Chinese Academy of Sciences, Beijing 100190, China
(Received 12 April 2015; published 17 June 2015)

We look into the signatures of the effective Y-bosonic strings in the gluonic profile due to a system of three static quarks on the lattice. The color field is calculated in pure SU(3) Yang-Mills lattice gauge theory at finite temperature with Polyakov loop operators. The analysis of the action density unveils a filled-Δ distribution. However, we found that these Δ-shaped action density profiles are structured from three Y-shaped Gaussian-like flux tubes. The geometry of the Y-shaped Gaussian flux tubes changes according to the quark configuration and temperature. The lattice data for the mean-square width of the gluonic action density have been compared to the corresponding width calculated based on the string model at finite temperature. We assume Y-string configuration with minimal length. The growth pattern of the action density of the gluonic field fits to junction fluctuations of the Y-baryonic string model for large quark separation at the considered temperatures.

DOI: 10.1103/PhysRevD.91.114506 PACS numbers: 12.38.Gc, 12.38.Aw, 12.38.Lg

I. INTRODUCTION

The confinement of quarks into mesons and hadrons is an outstanding feature of quantum chromodynamics (QCD). Computer simulations have revealed that quark confinement is a property of the gluonic sector and is common for non-Abelian gauge models [1–4]. The static quark-antiquark potential is linearly rising [5] with interquark separation. The origin of the linearly rising confining potential has been conjectured, in a stringlike flux tube model, to be due to the formation of a stringlike flux tube [6–12] between the two quark color sources.

The IR dynamics of the gluonic sector in the meson have shown gross features to be described in a string picture [7–12]. The squeezed flux tube, by virtue of the surrounding superconductiong medium [2,3,13], is conjectured to vibrate, after roughening, like a massless string. The profile of the vibrating flux tube can be unraveled in numerical lattice simulations by correlating the field strength of the QCD vacuum to the constructed quark states [14–17]. The large distance properties of the energy distribution in the meson have been a subject of many lattice simulations targeting the properties of the flux tubes at both zero and finite temperatures. The string picture's main measurable universal consequences of the Lüscher subleading correction to the $Q\bar{Q}$ potential [12] and flux tube logarithmic growth property [18] have been verified with the lattice data at large distances [4,9,14,19–22].

Nevertheless, the study of the stringlike behavior of flux tubes in multiquark systems seems to be less visited on the lattice. The calculations are prone to practical difficulties associated with both systematic and statistical uncertainties. The signal in the baryon is noisy [23], and the form of field distribution of the physically interesting ground state seems less obvious [23,24] than the mesonic case. There have been systematic difficulties to unravel an unbiased form of the action density distribution within the framework of the overlap formalism, i.e., employing Wilson loops as a quark source operator [23–25]. The gluonic wave function is reflected in the form of the field distribution [23–25]. This has presented hitherto a challenge to directly scrutinize unambiguously the baryonic strings on the lattice [26].

Our recent lattice Monte Carlo simulations, however, have unraveled the distribution of the gluonic gauge field inside a static baryon at finite temperature [27]. The action density correlation with three Polyakov loops, representing an infinitely heavy quark state in pure SU(3) Yang-Mills theory, has displayed a filled Δ-shaped profile [27,28]. This filled Δ-shaped arrangement interestingly persists to large interquark separations [27]. This varies the action density profile obtained using Wilson loops as a quark operator [23–25]. Wilson's loop operator displays three distinctive Y-shaped flux tube forms in the interquark space at large distances [25]. The returned gluonic pattern of the baryon with three Polyakov loops displayed a system rich with features [27,28] taking into account the role played by the temperature as well. The associated signatures of the string configuration relevant to this quark system [29,30] is indeed an interesting topic that remains to be addressed in detail.

Static color charges corresponding to a multiquark system may induce an intricate stringy system in the QCD vacuum including the formation of multijunction systems [31–34]. In tetraquark and pentaquark systems, the analysis of color fields show evidence on the formation of a multi-Y-type shaped flux tube [31,32]. The flux tube junction points are compatible with Fermat-Steiner points minimizing the total

---

[*] abakry@impcas.ac.cn

flux tube length [31,32]. In the baryon, the picture would simplify to the Y-string configuration which is expected to be a staple configuration in the IR region of the baryon [34]. This system accounts for three strings originating from a node to the three quarks [35]. The modeling of this system would entail utilizing collective coordinates referring to the junction location. Now we have a theoretical development relevant to the effective string effects in this model [29,30,36]. The calculations of the Casimir energy have indicated a Lüscher-like subleading term for the Y (3Q) potential [29,37]. There is also a discussion from a gauge-string perspective in Ref. [38].

In fact, a look at the signatures of the baryonic strings in lattice data simultaneously scrutinizes the subleading properties of the quark potential as well as the configuration of the strings that join the constituent quarks; or in other words, the leading term of the 3Q potential. The leading properties of the 3Q potential have been extensively studied on the lattice [39–42] employing various techniques. Recent lattice QCD findings regarding the three quark potential have shown that the confining potential admits two possible models depending on the interquark separation distances [39–43]. The so-called Δ parametrization for small quark separation distances of $R < 0.7$ fm and the Y ansatz for $0.7 < R < 1.5$ fm [41]. In fact, the distances over which the Δ and Y ansatz parametrization interpolates has been controversial for a long period of time [39–42] due to the small value in the difference between both ansatz (of the order of 15%) and the degree of accuracy of the data.

A direct test of the baryonic subleading string signatures in the lattice data for the potential of three static quarks at zero temperature has been reported in Ref. [37]. The numerical measurements of a three-state Potts gauge model is consistent with the predicted Lüscher-like corrections and the formation of a system of three flux tubes that meet at a junction when the separation between any two quarks is large [37].

In general, the lattice data are in favor of the expected Y-string configuration as the most relevant picture in the IR region of the baryon [44–47]. The quantum delocalization of this string system from its classical configuration results in a mean-square width of the flux distribution. Recently, the study of the dynamics of the junction of the three Y-shaped baryonic flux tubes has shown that the asymptotic behavior of the effective width of the junction grows logarithmically [30] with the distance between the sources. This result [30] is evaluated for equilateral triangular quark configurations at zero temperature. The result resembles the logarithmic growth property of the mesonic flux tubes [4,9,14,19–22] on the lattice.

The feasibility of reproducing lattice data corresponding to the gluonic pattern in a three-quark system at two temperatures below the deconfinement point presents a tempting opportunity to directly look into the baryonic strings in the properties of the QCD vacuum on a first principle basis. In addition to this, one would like to ascertain the interesting long distance Δ-shaped flux arrangement as a consequences of the stringy aspects of gluonic configurations of a static baryon. Since the bosonic string predictions are expected to be more relevant to pure Yang-Mills theories with static color sources (rather than QCD with dynamical sea quarks where string breaking [48] occurs), the lattice simulations are performed on the SU(3) gauge group in the quenched approximation.

In this work, we study the width profile of the junction due to a Y-string model [29,30,37] at finite temperature. The width pattern of the gluonic action density resulting from three different sets of 3Q configurations is investigated versus a variety of Y-shaped three string configurations obtained by varying the position of the junction. The fit analysis is performed at two temperatures corresponding to $T/T_c = 0.8$ and $T/T_c = 0.9$ which correspond to a temperature close to the end of the QCD plateau and to the deconfinement point, respectively.

The present paper is sectioned as follows: In Sec. II we describe the details of the simulations and noise reduction techniques. The baryonic string model at finite temperature is discussed in Sec. III. In Sec. IV, we show the properties of the density distribution and compare the profile of the mean width of the junction fluctuations for various string configurations to the width of the gluonic action density of the corresponding quark configurations at two temperatures. In Sec. V, the conclusion is provided.

II. MEASUREMENTS AND ULTRAVIOLET FILTERING

A. Color field measurements

The heavy baryonic state is constructed by means of Polyakov loop correlators,

$$\mathcal{P}_{3Q} = \langle P(\vec{r}_1)P(\vec{r}_2)P(\vec{r}_3)\rangle,$$

where the color-averaged Polyakov loop is given by

$$P(\vec{r}_i) = \frac{1}{3}\mathrm{Tr}\left[\prod_{n_t=1}^{N_t} U_{\mu=4}(\vec{r}_i, n_t)\right],$$

and the vectors $\vec{r}_i$ define the positions of the quarks.

The measurements that characterize the color field are taken by a gauge-invariant action density operator $S(\vec{\rho}, t)$ at spatial coordinate $\vec{\rho}$ of the three-dimensional torus corresponding to an Euclidean time t. The measurements are repeated for each time slice and then averaged,

$$S(\vec{\rho}) = \frac{1}{N_t}\sum_{n_t=1}^{N_t} S(\vec{\rho}, t). \tag{1}$$

A dimensionless scalar field that characterizes the gluonic field can be defined as

$$\mathcal{C}(\vec{\rho},\vec{r}_1,\vec{r}_2,\vec{r}_3) = \frac{\langle \mathcal{P}_{3Q}(\vec{r}_1,\vec{r}_2,\vec{r}_3) S(\vec{\rho})\rangle}{\langle \mathcal{P}_{3Q}(\vec{r}_1,\vec{r}_2,\vec{r}_3)\rangle\langle S(\vec{\rho})\rangle}, \tag{2}$$

where $\langle \ldots \rangle$ denotes averaging over configurations and lattice symmetries, and the vector $\vec{\rho}$ refers to the spatial position of the flux probe with respect to some origin. Due to cluster decomposition of the operators, C should approach a value $C \simeq 1$ away from the interquark space. For noise reduction, we make use of translational invariance by computing the correlation on every node of the lattice, averaging the results over the volume of the three-dimensional torus, in addition to the averaging of the action measurements taken at each time slice in Eq. (1).

The gauge configurations were generated using the standard Wilson gauge action. The two lattices employed in this investigation are of a typical spatial size of 3.6^3 fm^3. Performing the simulations on large enough lattice sizes would be beneficial to gain high statistics in a gauge-independent manner and also minimizing the mirror effects and correlations across the boundaries as a by-product [25,49].

The SU(3) gluonic gauge configurations has been generated employing a pseudo-heat-bath algorithm [50,51] updating the corresponding three SU(2) subgroup elements [52]. Each update step consists of one heat bath and five microcanonical reflections. We chose to perform our analysis with lattices as fine as $a = 0.1$ fm by adopting a coupling of value $\beta = 6.00$, with temporal extents of $N_t = 8$ and $N_t = 10$ slices, which correspond to temperatures $T \simeq 0.9T_c$ and $T \simeq 0.8T_c$, respectively.

We perform a set of measurements $n_{\mathrm{sub}} = 20$ separated by 70 sweeps of updates. Each set of measurements is taken following 2000 updating sweeps. These submeasurements are binned together in evaluating Eq. (2). The total measurements taken on 500 bins. In this investigation, we have taken 10,000 measurements at each temperature. The measurements are taken on hierarchically generated configurations.

B. Ultraviolet filtering

An ultraviolet filtering (UV) step precedes our measurements of the action density distribution throughout the lattice. The UV filtering of the gauge configurations suppresses the short distance quantum fluctuations of the vacuum and is beneficial in attaining a good signal to noise ratio in the correlations equation (2). This involves a local action reduction by smearing the gauge links of the whole four-dimensional lattice.

Smoothing the gauge fields complements our use of lattice symmetries to gain noise reduction in our measurement setup. We have shown previously [53] through a systematic study of the effects of smearing on the flux tube width profile that the effective string physics in the heavy meson is independent of the UV fluctuations at large source separations.

In addition to this, we have found the lattice data compares favorably with the predictions of the free string model with increasing the levels of gauge field smoothing at the intermediate source separation distance at high temperatures where the free string picture is known to poorly describe the flux tube width profile (see also a detailed discussion on the effects of smearing in [28]).

Variant to [16] where the Cabbibo-Marinari cooling has been employed, we have chosen to smooth the gauge field by an overimproved stout-link smearing algorithm [54]. In standard stout-link smearing [55], all the links are simultaneously updated. Each sweep of the update consists of a replacement of all the links by the smeared links

$$\tilde{U}_\mu(x) = \exp(iQ_\mu(x))U_\mu(x), \tag{3}$$

with

$$Q_\mu(x) = \frac{i}{2}(\Omega^\dagger_\mu(x) - \Omega_\mu(x)) - \frac{i}{6}\mathrm{tr}(\Omega^\dagger_\mu(x) - \Omega_\mu(x)),$$

and

$$\Omega_\mu(x) = \left(\sum_{\nu\neq\mu}\rho_{\mu\nu}\Sigma^\dagger_{\mu\nu}(x)\right)U^\dagger_\mu(x),$$

where $\Sigma_{\mu\nu}(x)$ denotes the sum of the two staples touching $U_\mu(x)$ which reside in the $\mu - \nu$ plane.

The scheme of overimprovement requires $\Sigma_{\mu\nu}(x)$ to be replaced by a combination of plaquette and rectangular staples. This ratio is tuned by the parameter ϵ [54]. In the following we use a value of $\epsilon = -0.25$, with $\rho_\mu = \rho = 0.06$. We note that for a value of $\rho = 0.06$ in the overimproved stout-link algorithm is roughly equivalent in terms of UV filtering to the standard stout-link smearing algorithm with the same $\rho = 0.06$. We have considered a typical number of four-dimensional smearing sweeps corresponding to $n_{sw} = 80$ of stout-link smearing.

III. BARYONIC STRING MODEL

In the dual superconductor model of the QCD vacuum, the QCD vacuum squeezes the color fields into a confining string dual to the Abrikosov line by the dual Meissner effect [2,3]. With this intuitive picture, an idealized stringlike system of flux tubes [12] transmitting the strongly interacting forces between the color sources was proposed previously [6,12]. The formation of stringlike defects is not a peculiar property of the QCD flux tubes, and is realized in many physical phenomena such as vortices in superfluids [56], flux tubes in superconductors [57], vortices in Bose Einstein condensates [58], Nielsen-Olesen vortices of field theory [59], and cosmic strings [60]. The physical parameters of each of these models fix the properties of this stringlike object.

However, quantum mechanical effects become relevant in certain phases of the model, giving rise to interesting measurable effects. To find a consistent quantum description within the quantization scheme used in bosonic string theories, we encounter the difficulty that this is only possible in 26 dimensions.

An effective description with strings [61] in four dimensions predicts logarithmic growth and a long non-Coulombic term to the quark-antiquark potential well known as the Lüscher term. These predictions have been verified in confining gauge theories on distance scales larger than the intrinsic thickness of the flux tube $1/T_c$ [20] at zero temperature in the so-called rough phase of lattice gauge theories (LGTs) [4,9,14,20,62].

The roughening transition signifies the substantial change in the behavior of the profile of the flux tube between a quark-antiquark pair from the constant width into logarithmic increase [18] by virtue of the strongly fluctuating underlying string. The transition proceeds with the decrease of the coupling constants and, in this phase, the flux tube admits a collective coordinate description.

At sufficiently high temperature, the equations of motion of a Nambu-Goto type bosonic strings are indicating a linear growth in the tube's width if solved [63] for the width of the action density at the middle plane between two quarks. This prediction has been also verified in LGTs by studying configurations with a static quark and antiquark pair [21,53,63–66] at large separations and near the deconfinement point. The string model assumptions of the effective description of the tube with a collective coordinate referring to the underlying thin string are working at high temperature.

The above discussion concerning the validity of the model assumption at high temperatures and near the deconfinement point is of particular relevance especially when discussing a Y-shaped baryonic string model [29,30,37] to scrutinize the large distance Δ baryonic flux arrangement [27,28].

It is widely accepted that the Y-shaped string is the relevant picture of the baryonic flux tubes to the IR region of the non-Abelian gauge and amounts to three squeezed flux tubes that meet at a junction. Indeed, it can be derived from the strong coupling approximation and is consistent with the dual superconducting picture of QCD [67–69]. The Y ansatz describes the leading string effect and can be successful for parametrizing the large distance lattice data of the confining potential [29,37] at zero temperature.

We summarize the motivation to discuss an effective Y-string model versus the lattice data at high temperature in the following main points: The linear growth property of the confining flux tube at high temperature has been verified on the lattice [21,53,63–66], no substantial changes [70] in the nature of the confining thin tubes between a quark-antiquark pair on large distance scales, and the Y model seems consistent with lattice data corresponding to the confining potential at $T = 0$ [37]. The expectations are that the observed features of the gluonic distribution may arise as a result of the vibration of this underlying Y-shaped string system.

In the Y-baryonic string model, the quarks are connected by three strings that meet at a junction (Fig. 1). The classical configuration corresponds to the minimal area of the string world sheets. Each string's world sheet (blade) consists of a static quark line and the worldline of the fluctuating [29,30] junction (Fig. 2).

The parameter s and t (time) label the position on string world sheet (blade) i. The position of the junction is given by $s = L_i + \eta_i.\phi(t)$. The transverse fluctuations $\xi_i(t,s)$ vanish at the location of the quarks ($s = 0$), and are periodic in the time t, with period $1/L_T$ (see Fig. 2) and is the temporal extent governing the inverse temperature.

The simplest choice for the string action S is the Nambu-Goto (NG) action which is proportional to the surface area

$$S[X] = \sigma \int d\zeta_1 \int d\zeta_2 \sqrt{g}, \tag{4}$$

where $g_{\alpha\beta}$ is the two-dimensional induced metric on the blade world sheet embedded in the background $\mathbb{R}^4$,

$$g_{\alpha\beta} = \frac{\partial X}{\partial \zeta_\alpha} \cdot \frac{\partial X}{\partial \zeta_\beta}, \qquad (\alpha, \beta = 1, 2), \qquad g = \det(g_{\alpha\beta}).$$

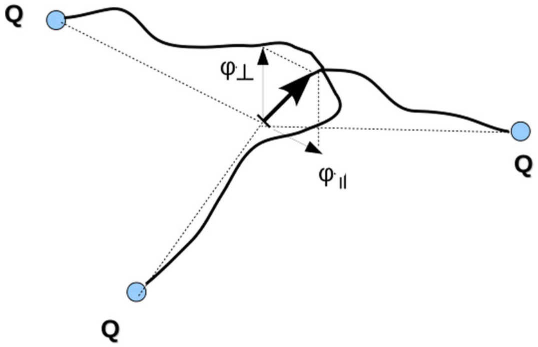

FIG. 1 (color online). Fluctuating Y-shaped flux tube arrangement of three static color sources Q. The junction position is described by the collective coordinate ϕ.

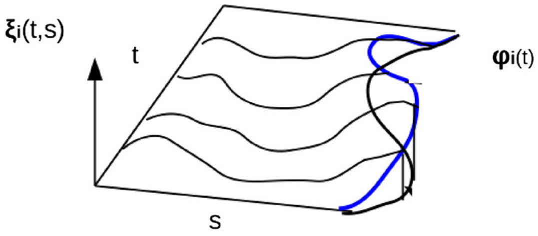

FIG. 2 (color online). World sheet traced by one of the strings up to the junction position.

The vector $X^{\mu}(\zeta_1, \zeta_2)$ maps the region $\mathcal{C} \subset R^2$ into R^4. Gauge fixing is required for the path integrals involving the string partition functions to be well defined with respect to Weyl and reparametrization invariance. The physical gauge $X^1 = \zeta_1, X^4 = \zeta_2$ would restrict the string fluctuations to transverse directions to $\mathcal{C}$. On the quantum level, Weyl invariance is broken in four dimensions, however, the anomaly is known to vanish at large distances [7]. The transverse fluctuations $X_{\perp} = \xi^{\mu}(t, s)$ vanish at the location of the quarks ($s = 0$), and are periodic in the time t, with period L_T, that is, the Dirichlet boundary condition in addition to the boundary condition from the continuity of the transverse fluctuations $\xi_i(t, s)$,

$$\xi_i(t, L_i + \eta_i \cdot \phi(t)) = \phi_{\perp i}(t), \tag{5}$$

where η_i are spatial unit vectors in the direction of the strings such that $\Sigma_i \eta_i = 0$. The NG action after gauge fixing and expanding around the equilibrium configuration yields

$$S_{\mathrm{Fluct}} = \sigma L_Y L_T + \frac{\sigma}{2} \sum_{i,j} \int_{\Theta_i} d^2\zeta \frac{\partial \xi_i}{\partial \zeta_j} \cdot \frac{\partial \xi_i}{\partial \zeta_j}, \tag{6}$$

where $L_Y = \sum_i L_i$ above denotes the total string length. In this model [29,30], the junction is assumed to acquire a self-energy term m. This results in an additional boundary term to NG action,

$$S = S_{\mathrm{Fluct}} + S_{\mathrm{Boundary}},$$

with a static energy and a kinetic energy terms of junction defined as

$$S_{\mathrm{Boundary}} = \left(m L_T + \frac{m}{2} \int_0^{L_T} dt |\dot{\phi}|^2 \right),$$

respectively.

The system's partition function then reads

$$Z = e^{-(\sigma L_Y + m) L_T} \int D\phi \exp\left(-\frac{m}{2} \int dt |\dot{\phi}|^2 \right) \prod_{i=1}^{3} Z_i(\phi), \tag{7}$$

where $Z_i(\phi)$ denotes the partition function for the fluctuations of a given blade that is bounded by the junction worldline $\phi(t)$:

$$Z_i(\phi) = \int_{\phi} D\xi_i \exp\left(-\frac{\sigma}{2} \int |\partial \xi_i|^2 \right). \tag{8}$$

The string partition functions $Z_i(\phi)$ are Gaussian functional integrals and can be calculated according to

$$Z_i(\phi) = e^{-\frac{\sigma}{2} \int |\partial \xi_{\mathrm{min},i}|^2} |\det(-\triangle_{\Theta_i})|^{-(D-2)/2} \tag{9}$$

where $\xi_{\mathrm{min},i}$ is the minimal-area solution for given $\phi(t)$. Δ_{Θ_i} denotes the Laplacian acting on the domain (blade) Θ_i. $\xi_{\mathrm{min},i}(t, s)$ is harmonic and satisfies the boundary conditions equation (5) [29].

Jahn and de Forcrand [29] calculated the baryonic potential, V_{qqq}, by evaluating the determinant of the Laplacian in Eq. (9) based on conformally mapping generalized domains of the blade [29].

Pfeuffer, Bali, and Panero [30] extended the calculations of the above model to the thickness of the fluctuating baryonic junction

$$\langle \phi^2 \rangle = \frac{\int D\phi \phi^2 e^{-S}}{\int D\phi e^{-S}}. \tag{10}$$

The integral over ϕ has been decomposed in Eq. (10) using parallel and perpendicular components $|\phi_{w,zi}|^2 = |\phi_w|^2 - |\phi_w \cdot \eta_i|^2$ to the plane of the quarks (see Fig. 1). This has resulted in an expression for the mean-square value of the perpendicular fluctuations [30] given by

$$\langle \phi_z^2 \rangle = \frac{2}{L_T} \sum_{w>0} \frac{1}{m w^2 + \sigma w \sum_i \coth(w L_i)}, \tag{11}$$

with $w = 2\pi n / L_T$.

The above equation is consistent with the mesonic string fluctuations in the limit $L_T \to \infty$. This can be shown by dividing the string connecting a quark and an antiquark into two parts of equal length connected in the middle by a junction, see Fig. 3. In the limit $L_T \to \infty$, for a three string system of identical lengths $L = L_i$, the perpendicular contribution in four dimensions would then read

$$\langle \phi_z^2 \rangle = \frac{1}{\pi\sigma} \int_0^{\infty} dw \frac{1}{m w^2 + n \sigma w \coth(w L)}. \tag{12}$$

To a leading order, the integral simplifies to

$$\langle \phi_z^2 \rangle = \frac{1}{\pi\sigma} \ln \frac{L}{L_0}. \tag{13}$$

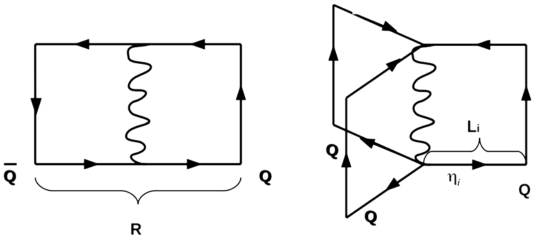

FIG. 3. Schematic shows the world sheets of the strings in a baryon and a meson. The solutions obtained for a single mesonic string [18,63] must be consistent with the general n-string baryonic solution [29,30] in the limit of strings number $n = 2$.

The arbitrary constant is contained in L_0, which generally will depend on the dimension and the number of strings and the ultraviolet properties of the corresponding gauge model [53]. This indicates that the width of the junction, orthogonal to the plane swept by the quarks, grows logarithmically with the distance.

One can relate Eq. (14) to the mean-square width, W_0^2, determined at the symmetry point of the string world sheet [18]

$$W_0^2 = \frac{1}{\pi\sigma} \ln \frac{R}{R_0}. \tag{14}$$

These equations coincide provided that the constants are identified as $L_0 = 2R_0$. The parameter m which has been absorbed into L_0, therefore, scales linearly with the parameter R_0.

The calculations performed in Refs. [29,30] is based on first order conformal mapping from the fluctuating side of the general domains Θ_i to a rectangle, then solving for the determinant of the Laplacian in Eq. (9) using the standard procedure [18]. For our further purpose, the approximation in Eq. (11) can be improved further by including the high temperature effects using a simple convolution with the first order fluctuations $\phi \to \int_{-\infty}^{\infty} \phi(\tau)\psi(t-\tau)d\tau$, that is, the fluctuating side of the general domains Θ_i describing the world sheet of each blade can be smoothed with a scalar function ψ such that the conformal mapping [29] would read

$$f_i(z) = z + \frac{1}{\sqrt{L_T}} \sum_{\omega=0} \frac{\eta_k.\phi_\omega \psi(\omega, L_i)}{\sinh(\omega L_i)} e^{\omega z}. \tag{15}$$

Following the same procedure as Ref. [30] for the calculation of the thickness of the junction (see Appendix A), the perpendicular fluctuations of Eq. (11) become

$$\langle \phi_z^2 \rangle = \frac{2}{L_T} \sum_{w>0} \frac{1}{kw^2 + \sigma w \sum_i \coth(wL_i)\psi(w, L_i)}. \tag{16}$$

The form of this convolution scalar ψ in the above equation can be derived from the mesonic limit. The width of the mesonic string derived in Ref. [63] at high temperature would read,

$$W^2(\xi_1, \tau) = \frac{1}{\pi\sigma} \log\left(\frac{R}{R_0}\right) + \frac{1}{\pi\sigma} \log|\chi(\tau)|, \tag{17}$$

where $\chi(\tau) = \frac{\theta_2(0;\tau)}{\theta_1'(0;\tau)}$, θ_1 and θ_2 are Jacobi theta functions, and $\tau = L_T/R$ is the modular parameter of the cylinder. Equating both expressions of Eqs. (16) and (17), with $R = 2L_i$, expanding the logarithm in the right-hand side and solving for $\psi(w, L_i)$ yields for the smoothing ψ the following expression:

$$\psi(w_n, L_i) = \frac{-kw_n}{2\sigma \coth(w_n L_i)} - \frac{(1 - 1/2n)}{2\coth(w_n L_i)} \times \left(\frac{2L_i\chi(\tau_i) + 1}{2L_i\chi(\tau_i) - 1}\right)^{2n-1}. \tag{18}$$

As indicated above, the parameter m shifts the mean-square width of the fluctuations by a constant. The parameter m can be tuned to the value k, such that R_0 cancels out from both sides of Eqs. (16) and (17).

After plugging the smoothing scalar ψ into the mean-square width of the in-plane fluctuations and orthogonalizing the corresponding path integral (Appendix A), we have

$$\begin{aligned}
\langle \phi_x^2 \rangle &= \frac{2}{L_T} \sum_{w>0} \frac{1}{Q_{x,w} + Q_{y,w} - (Q_{xy,w}^2 + (Q_{x,w} - Q_{y,w})^2)^{1/2}}, \\
\langle \phi_y^2 \rangle &= \frac{2}{L_T} \sum_{w>0} \frac{1}{Q_{x,w} + Q_{y,w} + (Q_{xy,w}^2 + (Q_{x,w} - Q_{y,w})^2)^{1/2}},
\end{aligned} \tag{19}$$

where Q_x, Q_y, and Q_{xy} are defined [30] as

$$\begin{aligned}
Q_x &= \left(kw^2 + \sigma w \sum_i \coth(wL_i)\psi(w, L_i)\right) + \left(\frac{\sigma}{2} w + \frac{w^3}{12\pi}\right) \left[\sum_i \eta_{i,x}^2 \coth(wL_i)\psi(w, L_i)\right], \\
Q_y &= \left(kw^2 + \sigma w \sum_i \coth(wL_i)\psi(w, L_i)\right) + \left(\frac{\sigma}{2} w + \frac{w^3}{12\pi}\right) \left[\sum_i \eta_{i,y}^2 \coth(wL_i)\psi(w, L_i)\right], \\
Q_{xy} &= \left(\frac{\sigma}{2} w + \frac{w^3}{12\pi}\right) \left[\sum_i \eta_{i,x}\eta_{i,y} \coth(wL_i)\psi(w, L_i)\right].
\end{aligned} \tag{20}$$

It is more convenient for our further discussion of the in-plane fluctuations on the lattice to consider the above rotated decoupled form.

IV. THE GLUONIC PROFILE AND BARYONIC STRINGS

In this section we show an analysis of the lattice data from two points of view. In the first subsection, we give a qualitative description of the rendered action density profile. We show how the aspects of the distribution are consistent with the stringlike behavior. We directly compare the width profile of the action density with the string model fluctuations, Eqs. (16), (18), and (19), in the following subsection.

A. Qualitative features

The simulation setup was described in Sec. II. The lattice operator which characterizes the gluonic field $\mathcal{C}$ is usually taken as the correlation between the vacuum lattice action density $S(\vec{\rho},t)$ operator, and a gauge-invariant operator representing the heavy baryon state, that is, three Polyakov lines [Eq. (2)]. We take our measurements with a three-loop field-strength tensor according to

$$F_{\mu\nu}^{\mathrm{Imp}} = \sum_{i=1}^{3} w_i C_{\mu\nu}^{(i,i)}, \tag{21}$$

where $C^{(i,i)}$ is a combination of Wilson loop terms corresponding to loops with lattice extent i used to construct the clover term and w_i are the corresponding weights [71].

Different possible components of the field-strength tensor in Eq. (21) can separately measure the chromoelectric and -magnetic components of the flux. The action density, however, is related to the chromoelectromagnetic fields via $\frac{1}{2}(E^2 - B^2)$ and is the quantity of direct relevance to the comparison with the string fluctuations, Eqs. (16) and (19).

The reconstructed action density

$$S(\vec{\rho}) = \beta \sum_{\mu>\nu} \frac{1}{2} \mathrm{Tr}(F_{\mu\nu}^{\mathrm{Imp}})^2 \tag{22}$$

is accordingly measured on 80 sweeps of stout-link smearing. The action density operator is calculated through an $\mathcal{O}(a^4)$ improved lattice version of the continuum field-strength tensor, Eq. (21). For convenience, we consider the complementary distribution $\mathcal{C}' = 1 - \mathcal{C}$ in the following. The correlation function Eq. (2) is found $\mathcal{C}'(\vec{\rho}) = 0$ away from the quark position.

The surface plot of the scaled flux distribution in the quark plane, $\rho(x,y,z=0)$, together with contour lines is plotted in Fig. 4. The contour lines are projected onto the surface plot. The density of the contour lines increases near the edges in accord with the gradient of the scalar field $\mathcal{C}'$ along the x axis. The flux contours corresponding to the highest values of $\mathcal{C}'$, however, are the innermost lines inside the triangle.

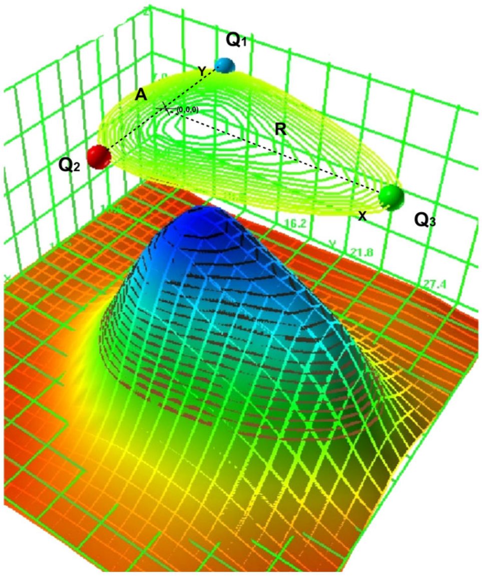

FIG. 4 (color online). Surface plot of the flux density surface in the quark plane, $\rho(x,y,z=0)$, together with contour lines. These measurements are taken for an isosceles quark geometry of base $A = 0.8$ fm, height $R = 1.2$ fm and temperature $T/T_c = 0.9$. The projected contour lines appear denser at the edges due to the fast gradient of the scalar field near the edges.

In general, the action density distribution is nonuniformly distributed. The distribution $\mathcal{C}'(\vec{\rho}(x,y,z=0))$ has an action density maximal curve along the middle line $\vec{\rho}(x,y=0,z=0)$ between the two quarks $Q_{1,2}$. With the increase of source Q_3 separation, the peak point along the maximal curve $\mathcal{C}'(\vec{\rho}(x,y=0,z=0))$ shows only subtle movement [27,28].

At large distances, the topology of these density plots does not indicate an action density pattern resembling the shape of tubes that would form around the perimeter of the three quarks. The distribution displays a peak close to the geometrical center of the triangle at large source separation distance. This is consistent with what we expect from the vibrations of three stringlike flux tubes that meet at a junction. The thin Y-shaped flux tube may delocalize away from its classical configuration and span the whole region throughout the bulk of the triangular 3Q arrangement, tracing out a filled-Δ shape of a nonuniform action density distribution with a maximal inside the triangle.

The nature of the forces that binds the nucleon is usually explored directly in lattice simulations via the fit behavior of a prescribed ansatz to the 3Q potential. The Δ ansatz amounts for a two-body force between the quarks proportional to the perimeter of the 3Q triangle with a string tension half that of the corresponding $q\bar{q}$ system. In the Y ansatz the string tension is, however, the same as the $q\bar{q}$ system. The force is a three-body force and is proportional to the minimal length of the three strings.

At zero temperature, the results seem to indicate a range for Δ-ansatz parametrization for small quark separation distances $R < 0.7$ fm, and the Y ansatz for $0.7 < R < 1.5$ fm [41,43]. In perturbation theory [72,73], the breakdown of the two-particle (Coulombic) interaction picture in the short range happens at two-loop order when the first genuine three-body force manifest.

It can be a point of subtlety, nevertheless, if the parametrization which provides the best possible fits of the data corresponding to the 3Q system potentials and the profile of the flux tubes are thought to be necessarily the same. Our lattice results for the profile of the flux tube [27,28] indicates a Δ-shaped flux profile at larger distances. In the following we shall show how the Δ-shaped flux configuration consists of three overlapping Y-shaped Gaussian flux tube "strings."

The analysis of the fit behavior of the action density profile can directly unravel the relevant stringlike configuration amongst certain quark configuration. The best choice of the fitting functions should be based on our experience of what the good fit of the action density profile for a single string would look like. For simplicity, we adopt the approximation where the action density distribution due to a delocalization of a single string can fit to a Gaussian form [20]. This is compatible with the accuracy of our lattice data shown also previously in the case of the mesonic flux tubes [53], for example.

To unravel the configuration of the strings, we explore the structure of the gluonic distribution with a general ansatz consisting of two Gaussians,

$$G(y) = H/2\exp(-(y-u)^2/W^2) + H/2\exp(-(y+u)^2/W^2). \qquad (23)$$

The form assumes a region consisting of a system of two overlapping strings of the same strength $H/2$, and mean-square width W^2. The center of the two strings is separated by distance $|2u(x)|$. This form make use of the symmetry of the flux tube arrangement and seems suitable to unveil the underlying string configuration. We scan the gluonic domain with the above fit function for all the distances x from the base A connecting the quarks Q_1 and Q_2. That is, the Gaussian fits to the action density data are performed for x_i transverse planes between two sources separated by a distance of R from the base up to the third quark Q_3.

The returned values of χ^2 to the fit of the form in Eq. (23) at some selected planes and quark configuration are summarized in Tables I and II for the temperature $T/T_c = 0.8$ and $T/T_c = 0.9$, respectively. Figures 5 and 7 illustrate the resultant fits to the sum of two Gaussians. The fit parameter $u(x)$ returns a nonzero value for fits of the first few planes from the base of the 3Q quark's triangle. The distance between the two Gaussians decreases as we move away towards the third quark position. The interesting behavior of the returned fit parameter $u(x)$ would be at the locus x_0 where the separation between the two strings vanishes, $u(x_0) = 0$. We refer to this point as the mean location of the junction which, as we shall see, can be delocated with at most two lattice spacings from the position of the Fermat point of the configuration for the temperatures near the deconfinement point.

TABLE I. The returned values of the χ^2_{dof} from the fits of the formula in Eq. (23) to the in-plane action density $\mathcal{C}'(\vec{\rho}(x_i, y, 0))$ at each x_i, at temperature $T/T_c = 0.8$.

(a) $R = 6a$

A/x	$x = 1$	$x = 2$	$x = 3$	$x = 4$	$x = 5$
$A = 6a$	1.7	1.6	1.9	4.8	6.7
$A = 8a$	0.4	0.3	0.2	0.5	0.8
$A = 10a$	0.3	0.2	0.3	0.1	0.6

(b) $R = 9a$

A/x	$x = 1$	$x = 2$	$x = 3$	$x = 5$	$x = 8$
$A = 6a$	1.0	0.8	0.8	1.5	1.2
$A = 8a$	0.8	0.2	0.3	0.5	0.2
$A = 10a$	0.6	0.4	0.3	0.2	0.2

TABLE II. Similar to Table I; however the returned values of χ^2_{dof} are for the temperature $T/T_c = 0.9$.

(a) $R = 6a$

A/x	$x = 1$	$x = 2$	$x = 3$	$x = 4$	$x = 5$
$A = 6a$	5.4	3.4	7.1	13.6	19.9
$A = 8a$	3.3	1.9	1.2	3.8	15.4
$A = 10a$	1.8	1.6	0.9	2.3	9.11

(b) $R = 9a$

A/x	$x = 1$	$x = 2$	$x = 3$	$x = 5$	$x = 8$
$A = 6a$	3.7	2.1	2.3	4.1	14.2
$A = 8a$	2.2	1.7	0.84	2.9	12.2
$A = 10a$	0.48	0.46	0.4	0.66	7.4

(c) $R = 11a$

A/x	$x = 1$	$x = 3$	$x = 5$	$x = 7$	$x = 9$
$A = 6a$	1.0	1.1	2.1	3.7	9.5
$A = 8a$	1.3	0.4	0.5	2.4	6.29
$A = 10a$	0.28	0.18	0.1	1.2	3.8

The values of the returned fit parameter $u(x_i)$ are plotted in Figs. 8 and 9 for temperatures $T/T_c = 0.8$ and $T/T_c = 0.9$, respectively. The coordinates (Lattice units) are measured from the quark position $x = 0$.

On the other hand, the perpendicular action density $\mathcal{C}'(\vec{\rho}(x_i, 0, z))$ when fitted to Eq. (23) shows no string splitting, that is, $u(x) = 0$ for all $x \in [0, R]$. Figure 10 illustrates fits to a single Gaussian form at various planes x in the plane perpendicular to the three quarks at $T/T_c = 0.8$. The values of χ^2_{dof} for the fits of the perpendicular action density $\mathcal{C}'(\vec{\rho}(x_i, 0, z))$ are of the same order as that shown in Tables I and II. At higher

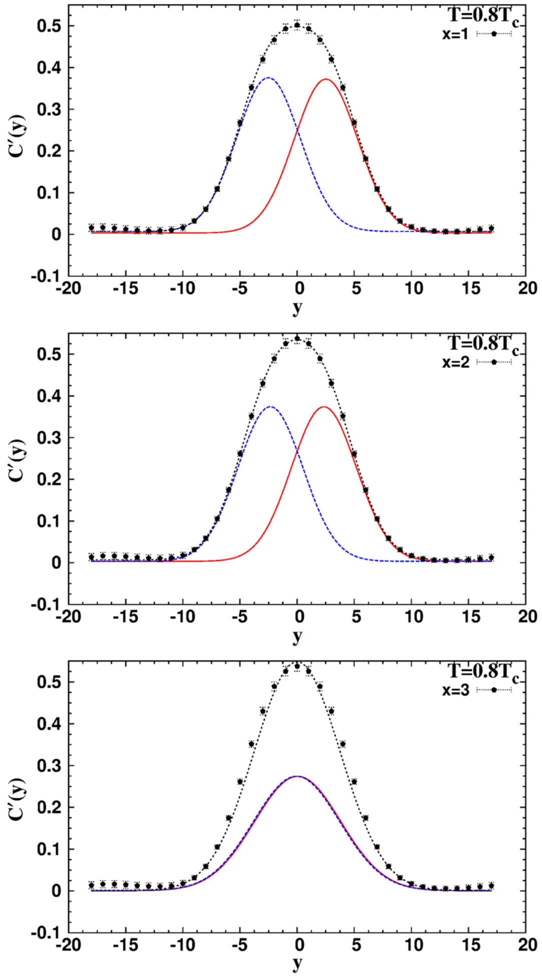

FIG. 5 (color online). The density distribution $\mathcal{C}'(\vec{\rho})$ for the isosceles configuration with the base, $A = 1.0$ fm, and height $R = 0.7$ fm at $T/T_c = 0.8$. Data are plotted for the transverse planes $x = 1$ to $x = 3$. The lines correspond to fits of the two Gaussians form Eq. (23) to the density in each plane $\vec{\rho}(x_i, y, 0)$. The distance between the two Gaussians gets closer, and they ultimately coincide at $u(x) = 0$ as we move into farther planes from the base of the triangle.

temperatures and smaller quark separation the signal is stronger and this leads to higher values of $\chi^2_{\rm dof}$. The first row in Tables I and II shows higher values of $\chi^2_{\rm dof}$ for the shortest triangular base $A = 6a$, especially for planes close to the third quark Q_3 position. This is also the case for the perpendicular fluctuations (higher $\chi^2_{\rm dof}$ for $A = 0.6$ and $T/T_c = 0.9$).

In Ref. [74] a fit convoluting a Gaussian with an exponential given by

$$G(z) = He^{2\kappa/\lambda}e^{(-2\sqrt{(z^2+\kappa^2)}/\lambda)}, \tag{24}$$

to measure both the string fluctuation and the screening effects, was used. With the employment of this ansatz, the flux tube damping is measured by means of the so-called penetration length λ and the central curvature radius

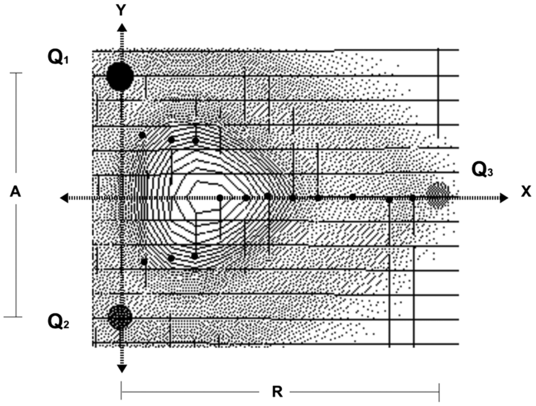

FIG. 6. The contour map of the action density at $T/T_c = 0.8$. The distance between Q_1 and Q_2 at the base of the triangle is denoted A, and R is the distance between the third quark Q_3 and the base. The dots denote the locus of the center of the two Gaussians, Eq. (23).

$-2H/(\lambda\kappa)$ [74], the additional parameter κ is an effective distance. The ansatz equation (24) accounts for screening effects pronounced at the tail of the flux tube profile and can lead to better $\chi^2_{\rm dof}$ values. We fit the above convolution form Eq. (24) to the perpendicular action density $\mathcal{C}'(\vec{\rho}(x_i, 0, z))$. The resultant values of $\chi^2_{\rm dof}$ are summarized in the second row of Table III.

The values in Table III show a remarkable reduction in $\chi^2_{\rm dof}$ for the above mentioned quark configuration and thus signaling possible screening effects to be observed in the present analysis. However, for other quark configurations and lower temperatures, the signal strength characterized by the size of the error bars on the measured action density may not be sufficient to further isolate the screening from the quantum widening [74]. We expect screening effects to be more feasible to scrutinize for the profile of a single mesonic string as well as the string due to the diquark quark, since the signal is relatively easier to improve and the flux tube system is simpler. We report this in detail elsewhere.

At $T/T_c = 0.8$, the two strings show an obvious splitting behavior, as can be seen in Fig. 8. The position of the point of intersection $u(x_0) = 0$ is the closest plane to the Fermat point of this quark configuration. The point of intersection relocates at most one lattice spacing $x_0 + 1$ for large triangle height R and bases $A = 8a, 10a$, respectively. The positions of the centers of the two Gaussians of Eq. (23) have been superimposed on the contour density plot of Fig. 6.

The separation between the centers of the two strings is larger at the other temperature nearer to the deconfinement point $T/T_c = 0.9$. The point of intersection appears to be delocated two lattice spacings off the Fermat point of the configuration and still shows a subtle movement $x_0 + 1$ as the third quark is pulled away from the base.

Figure 11 plots the action isolines in the 3Q plane for the temperature closer to deconfinement point $T/T_c = 0.9$.

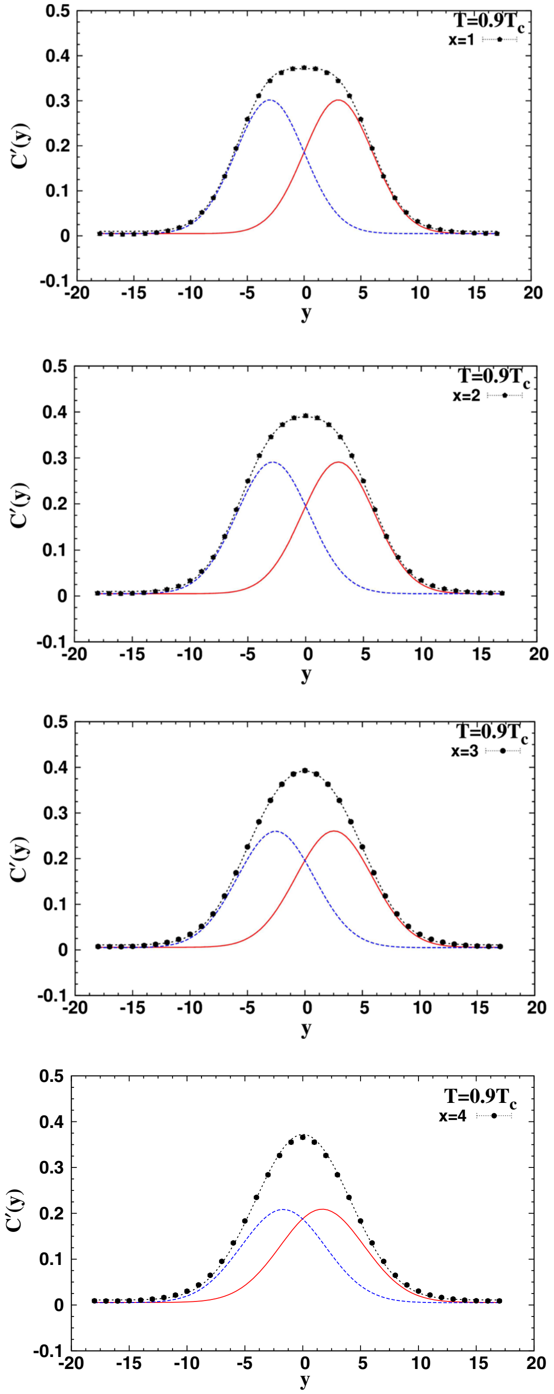

FIG. 7 (color online). Same as Fig. 5, the density distribution $\mathcal{C}'(\vec{\rho})$ for the isosceles configuration with the base, $A = 1.0$ fm, and height $R = 0.7$ fm at $T/T_c = 0.9$, respectively. Data are plotted for the transverse planes $x = 1$ to $x = 4$.

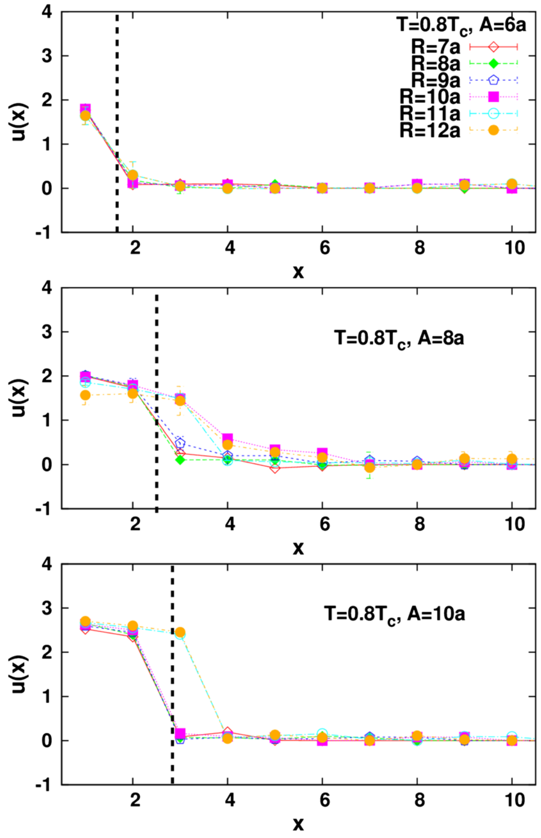

FIG. 8 (color online). The separation $u(x)$ between two Gaussians as in Figs. 5 and 7 used to fit the action density to Eq. (23). Each curve corresponds to $u(x)$ for each third quark Q_3 position of the isosceles with the base $A = 6a$, $A = 8a$, and $A = 10a$ at temperature $T/T_c = 0.8$. The legend (in the upper right corner) signifies the third quark position. The vertical dashed line denotes the position of the Fermat point of the configuration.

The lines superimposed on the density plot refer to the best fits to the position of the center of each of the two overlapping Gaussians in Eq. (23) based on the returned values of the separation parameter $u(x)$, see Figs. 5 and 7, for example. At small separation the positions of the junction are very close to the third quark position. The mean position of the strings seems to trace a circumference which looks like a Δ shape.

A shot of the profiles of the strings for the temperature nearer the deconfinement point and the other temperature at the end of the QCD plateau region is shown in Fig. 12. For the latter, the junction position is the closer to the Fermat point of the configuration. This indicates that the Y-Gaussian-like system has a maximal length near the deconfinement point before the strings ultimately break in the deconfinement phase. At all considered planes, the separation between the two strings, $u(x_i)$, increases with the increase of the temperature, indicating that the profile of the centers of the two Gaussians describes a mean location which is consistent with the spread of the gluonic energy with the increase of the temperature and source separation as well. Indeed, the measurements of the string tension at both temperatures show significant change [75].

The point of intersection at $T/T_c = 0.9$ does not coincide with the center of the contour circles in Fig. 12. Figure 13 shows that the position of the maximum of the action density does not also correspond to the

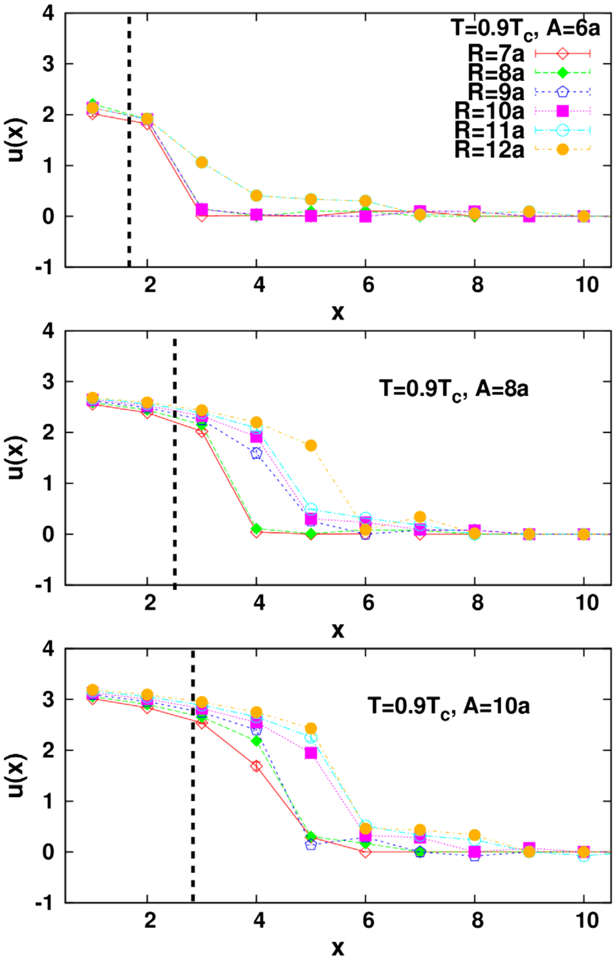

FIG. 9 (color online). Similar to Fig. 8, however for temperature $T/T_c = 0.9$. Each curve corresponds to $u(x)$ for each third quark Q_3 position of the isosceles with the base $A = 6a$, $A = 8a$, and $A = 10a$. The legend (in the upper right corner) signifies the third quark position.

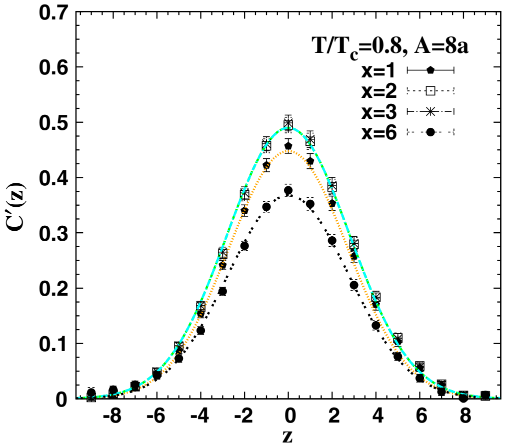

FIG. 10 (color online). The density distribution $\mathcal{C}'(\vec{\rho}(x,0,z))$ in the plane perpendicular to the 3Q plane for an isosceles configuration with the base, $A = 8.0$ fm, and height $R = 0.8$ fm at $T/T_c = 0.8$. The lines show the best fit to a Gaussian form.

TABLE III. Compares the returned values of χ^2_{dof} for a fit of the perpendicular action density $\mathcal{C}'(\vec{\rho}(x_i,0,z))$ at the temperature $T/T_c = 0.9$ to the Gaussian ansatz of Eq. (23) and the ansatz equation (24) Gaussian combined with an exponential [74].

(a) $R = 9a$

Plane	$x = 1$	$x = 2$	$x = 3$	$x = 5$	$x = 7$
Eq. (23)	6.4	5.2	4.4	3.9	4.45
Eq. (24)	0.3	0.3	0.3	0.2	0.2

intersection position $u(x_0) = 0$, at the temperature $T/T_c = 0.9$. At this temperature, the energy density assumes a more flat profile in the inner region close to the base. This is not the case at the other temperature, $T/T_c = 0.8$, where a sharper maximum of the action is closer to both the intersection and Fermat points.

In Figs. 11 and 12, there is a very interesting trend for the three fundamental strings to join at $120° = 2/3$ angles, even when the static charges are at different angles. Figure 12 shows that these tendencies to preserve equal angles at the node position exists at both temperatures. Together with the observation of the above indicated flatter action density profile near the deconfinement point, this could suggest a repulsion between the three fundamental strings to conform with equi-angles at the node position. We remark also on the simulations of the flip-flop model in Refs. [31,32], where the strings connect the color charges such that the total length of the strings is minimal with three elementary flux tubes meeting in a Fermat-Steiner point at an angle of 120°.

The transverse profile of the action density fits to a double humped function indicating a system of overlapping stringlike flux tubes. The revealed configurations of these Gaussian flux tubes show dynamical aspects and reconfigures with respect to the quark configuration and temperature.

Let us point out a third qualitative aspect related to the width of the gluonic action profile of the 3Q system that can have a stringy character. The gluonic flux in the 3Q system does not exhibit a symmetry between the width measured in the quark plane and that in the perpendicular direction. The flux strength distribution revealed with the action density using the Wilson loop does not appear to produce an asymmetric gluonic pattern. In Ref. [25] the radius of the tube is calculated with cylindrical coordinates assuming a cylindrical symmetry of the tube.

The second moment, $W^2_y(x)$, is measured by means of the fits to Eq. (23):

$$W^2_y(x_i) = \frac{\int dy y^2 \mathcal{C}'(\vec{\rho}(x_i,y,0))}{\int dy \mathcal{C}'(\vec{\rho}(x_i,y,0))}. \tag{25}$$

Tables VIII and IX in Appendix C list our measurement of the width of the flux tube for the in-plane action density,

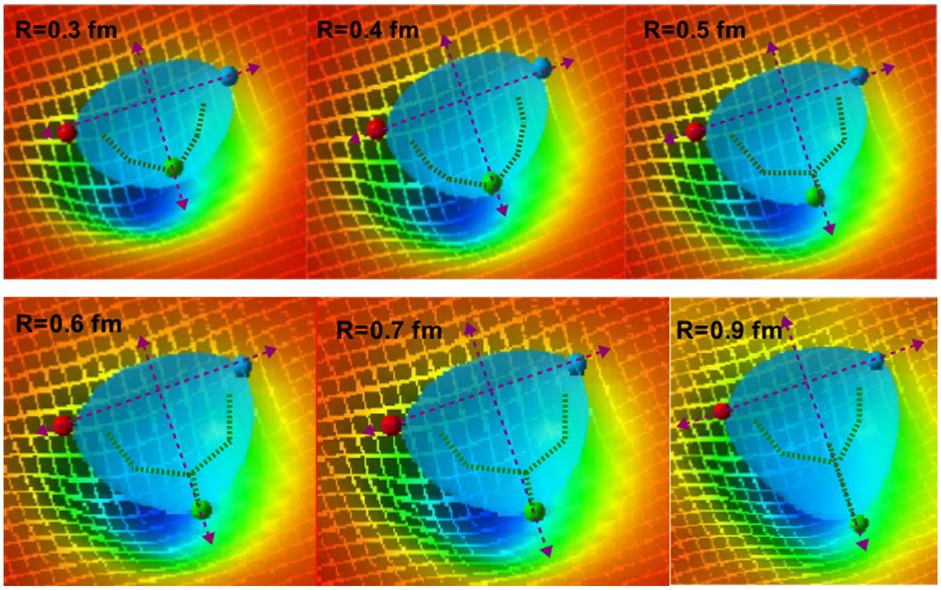

FIG. 11 (color online). The action density isolines in the (3Q) plane together with the lines connecting the center position of each Gaussian in the fit in Eq. (23). Each sphere denotes the quark position.

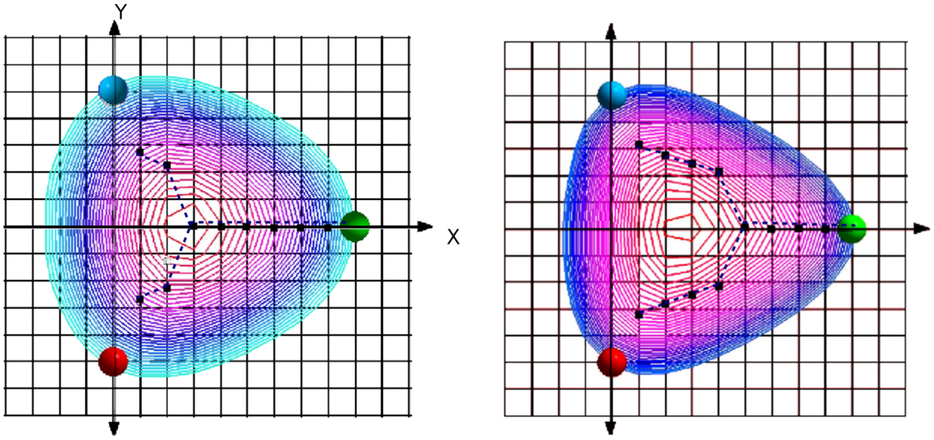

FIG. 12 (color online). This plot shows that the notable change on the profile of the baryonic flux arrangement, with the temperature increase, is the movement of the junction to the inner region of the quark configuration.

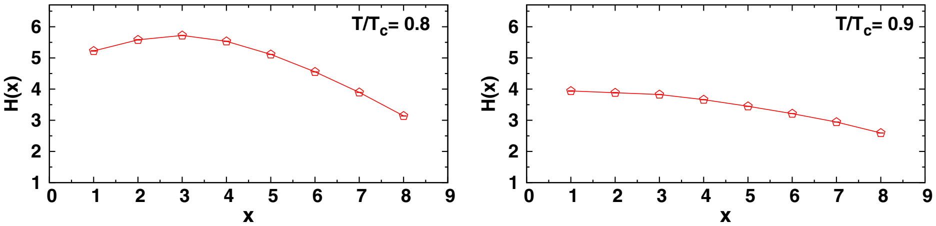

FIG. 13 (color online). The profile of the amplitude of the action density $H(x_i) = \mathcal{C}'(x; y = 0)$ along the $y = 0$ axis (scaled by a factor of 10) for each temperature of the quark configuration shown in Fig. 12.

for the isosceles configurations with base $A = 0.6$ fm, $A = 0.8$ fm, and $A = 1.0$ fm at two temperatures, $T/T_c = 0.8$ and $T/T_c = 0.9$, respectively. In Ref. [28] we have taken our width measurements using a single Gaussian form. Tables XI and XIII show the percentage difference between both width measurements. We note that the difference in width measurements is more pronounced for large quark separations at the higher temperature near

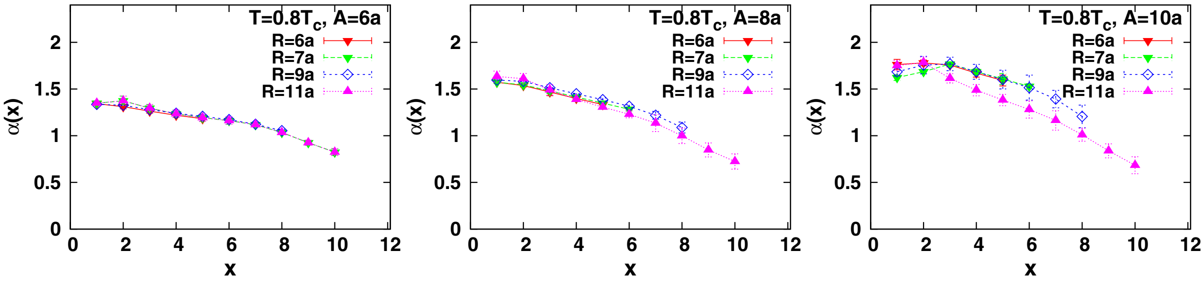

FIG. 14 (color online). Comparison of the ratio, α, of the mean squared width of the flux parallel and perpendicular to the quarks' plane for three isosceles bases $A = 0.6$ fm, $A = 0.8$ fm, and $A = 1.0$ fm at $T/T_c = 0.9$.

the deconfinement point and for the closest planes to the base of the triangles Q_1 and Q_2.

The string picture indicates an asymmetry in the mean square width between the two planes [30]. We compute this ratio of the action density in the two perpendicular planes based on fits to the form in Eq. (23). The width of the tube in the perpendicular direction is measured through Gaussian fits as

$$W_z^2(x_i) = \frac{\int dz z^2 \mathcal{C}'(\vec{\rho}(x_i, 0, z))}{\int dz \mathcal{C}'(\vec{\rho}(x_i, 0, z))}. \qquad (26)$$

Tables X and XII included in Appendix C list our measurement of the width of the flux tube for the perpendicular plane action density, for the isosceles configurations with base $A = 0.6$ fm, $A = 0.8$ fm, and $A = 1.0$ fm at two temperatures, $T/T_c = 0.8$ and $T/T_c = 0.9$, respectively.

We measure the aspect ratio between the width in the quark plane and that in the perpendicular plane to the quarks according to

$$\alpha(x) \equiv \frac{W_y^2(x)}{W_z^2(x)}. \qquad (27)$$

We plot in Fig. 14 the aspect ratio at the temperature $T/T_c = 0.8$ for the indicated quark configurations. Generally, the aspect ratio is greater than 1 for planes $x \in [0, 8]$, indicating that in-plane fluctuations are greater than the perpendicular fluctuations. This result is consistent with a greater restoring forces in the quark planes for the Y-stringlike gluonic distribution.

The aspect ratio increases with the base length and decreases, however, as we move up through the planes to the third quark position. With the increase of the base length parameter of the 3Q triangle, the split between the two strings is larger, giving rise to a larger width of the fluctuations. For the perpendicular direction, on the other hand, values in Table XII show smaller growth in the mean-square width with the base compared to the parallel width. The aspect ratio tends to assume closer values to 1 at those planes x larger than 8 lattice units from the base. This can be a consequence of the reduction in the effects of the junction's system as we move the third quark source farther from the base.

B. Broadening aspects

In the following the broadening of the flux tube is compared to the corresponding string model predictions. Formulas in Eqs. (16) and (19) shown in the last section account for the tube's mean-square width for both the in-plane and the perpendicular direction to the 3Q plane, respectively. A study of the fit behavior of each separate component can provide an indication on the compatibility of the baryonic string model with the measured LGT junction profile.

The Y string's configuration has to be fixed before proceeding to fits with the lattice data. Figure 15 demonstrates the proposed string configuration with respect to the quark positions. We focus our analysis on the flux tube's action density due to the 3Q planar configuration corresponding to isosceles triangles with bases of length $A = 6a$, $A = 8a$, and $A = 10a$. The locus of the junction x_f is fixed at the Fermat point of the isosceles triangle, i.e., a point such that the total distance from the three vertices of the triangle to this point is the minimum possible. The isosceles triangular configurations have the property of having the same locus of the Fermat point. The position of the Fermat point does not depend on the height R of the triangle, and is given by $R = A/(2\sqrt{3})$. This planar quark setup is convenient to simplify the study of a baryonic junction on a lattice structure.

The measured values in Table VIII for the in-plane width profile are indicating a growth in the tube's mean-square

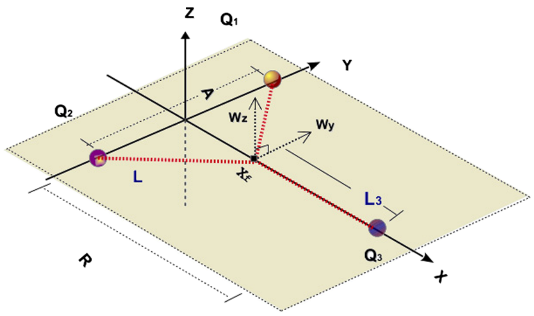

FIG. 15 (color online). Schematic diagram shows the position of the quarks and the configuration of the Y tring. The junction's position, x_f, is fixed at the Fermat point [29,30].

width at the first four transverse planes $x = 1$ to $x = 4$ as the third color source Q_3 is pulled apart. The growth in the flux tube width could be compared to the corresponding growth in the junction fluctuation in Eq. (16) and also Eq. (19) for the perpendicular fluctuations. Since the junction's fluctuations are nonlocal, this comparison can be performed by fitting the formula of Eqs. (16) and (19) at each selected transverse plane to the tube's measured widths. Here, we focus our analysis on the first four planes from the base of the quark triangle.

Let us first fit the measured lattice data for the in-plane width profile W_x^2 at the temperature $T/T_c = 0.8$ to Eq. (19). Table IV summarizes the returned values of $\chi^2_{\text{dof}}(x)$ from resultant fits to the indicated separation range R at four consecutive transverse planes $x = 1$ to $x = 4$.

In general, the fits show strong dependency on the fit range, especially with the inclusion of the points at small Q_3 source separations. Also high values of χ^2_{dof} are returned when fits include the entire considered range of sources' separations, i.e., $R = 5a$ to $R = 12a$. However, the values of χ^2_{dof} rapidly decrease when excluding those points at short distance separations. The fit reaches acceptable values starting with $\chi^2_{\text{dof}} = 1.4$ for widths measured at the plane $x = 1$ for isosceles triangles' quark configuration with bases of length $A = 6a$ at third source Q_3 separations $R = 6$ fm. However, the triangular configuration of base lengths $A = 8a$ and $A = 10a$ returns good values of $\chi^2_{\text{dof}} = 1.3$ and 1.6 for planes $x = 1$ and $x = 2$, respectively. The best fits for the triangle configuration with base lengths $A = 8a$ are obtained for Q_3 separations $R > 6a$ at the plane x_1. It is apparent that best fits shift one lattice spacing, that is $x = 2$, when the length of the triangle base parameter is increased to $A = 10a$, and the best fit is returned with Q_3 source separation $R > 7a$.

The existence of particular planes at which the above indicated best matches with the formulas of Eq. (19) suggests that some planes may receive a larger contribution of the junction's fluctuations than others. Figure 16 plots χ^2_{dof} for selected fit regions at planes $x = 1$ to $x = 4$. As mentioned above, the plane at which we obtain the minimal in χ^2_{dof} depends on the length of the base of the triangular isosceles quark configuration.

The positions of the Fermat point of the three isosceles of bases $A = 6a$, $A = 8a$, and $A = 10a$ would be $x_f = 1.7a$, $x_f = 2.3a$, and $x_f = 2.9a$, respectively. Recall that the Y-string configuration which we fit to the lattice data is such that the position of the junction is fixed at the Fermat point at both considered temperatures. One may expect, accordingly, that those planes closer in position to the string's junction (see Fig. 15, the configuration to which we fit the width profile) can provide better fits to the lattice data. We observe, however, that the planes of the best fits manifest in accord with the profile of the two Gaussians shown in Figs. 8 and 9 rather than junction's classical position at the Fermat point. For the in-plane fluctuations of Eq. (19), the

TABLE IV. The returned values of the $\chi^2_{\text{dof}}(x)$ corresponding to fits of the in-plane width $W_y^2(x)$ of the action density at each plane x to the string model formula in Eq. (19), the fits are for the isosceles triangle quark configuration of base $A = 6a$, $A = 8a$, and $A = 10a$ at $T/T_c = 0.8$.

(a) $A = 6a$

Fit range	4–10	4–13	5–13	6–13	7–13	8–13	9–13
$\chi^2_{\text{dof}}(1)$	31.8	21.5	4.9	1.38	1.03	1.2	1.1
$\chi^2_{\text{dof}}(2)$	5.6	5.2	3.9	4.9	5.4	5.6	5.2
$\chi^2_{\text{dof}}(3)$	64.1	44.9	7.8	4.3	5.1	5.1	4.5
$\chi^2_{\text{dof}}(4)$			3.8	3.9	4.1	4.0	3.5

(b) $A = 8a$

Fit range	5–9	06–10	5–12	6–12	7–12	8–12	9–12
$\chi^2_{\text{dof}}(1)$	5.7	5.7	12.11	4.5	1.3	1.15	0.3
$\chi^2_{\text{dof}}(2)$	25.0	25.0	64.4	19.9	5.3	1.1	0.2
$\chi^2_{\text{dof}}(3)$	18.1	18.1	49.2	15.5	4.9	3.2	3.4
$\chi^2_{\text{dof}}(4)$	10.6	10.6	35.5	10.6	7.3	4.1	2.5

(c) $A = 10a$

Fit range	5–9	5–11	6–12	7–12	8–12	9–12	10–12
$\chi^2_{\text{dof}}(1)$	30	41.8	22.3	8.5	2.4	0.7	0.3
$\chi^2_{\text{dof}}(2)$	47.9	21.9	15.7	1.6	0.7	0.11	0.07
$\chi^2_{\text{dof}}(3)$	600	487	152	37	11	2.5	0.2
$\chi^2_{\text{dof}}(4)$	159.9	128.9	48.3	22.1	11.05	3.7	2.1

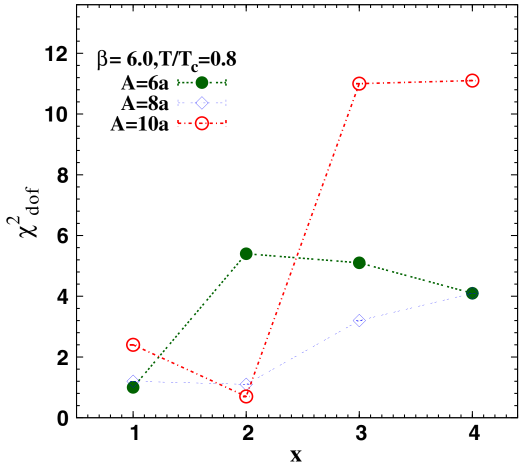

FIG. 16 (color online). Plots χ^2_{dof} of selected planes and ranges from Table IV for the isosceles base $A = 0.6a$, $A = 0.8a$, and $A = 1.0a$. The values for the same base length parameter are joined with dashed lines for illustration. The plotted χ^2_{dof} values are plane $x = 1$ corresponding to the base parameters $A = 0.6a$, and $x = 2$ for $A = 8a$ and $A = 10a$. The smooth line connects values of χ^2_{dof} belonging to the triangular configuration of the same position of the Fermat point.

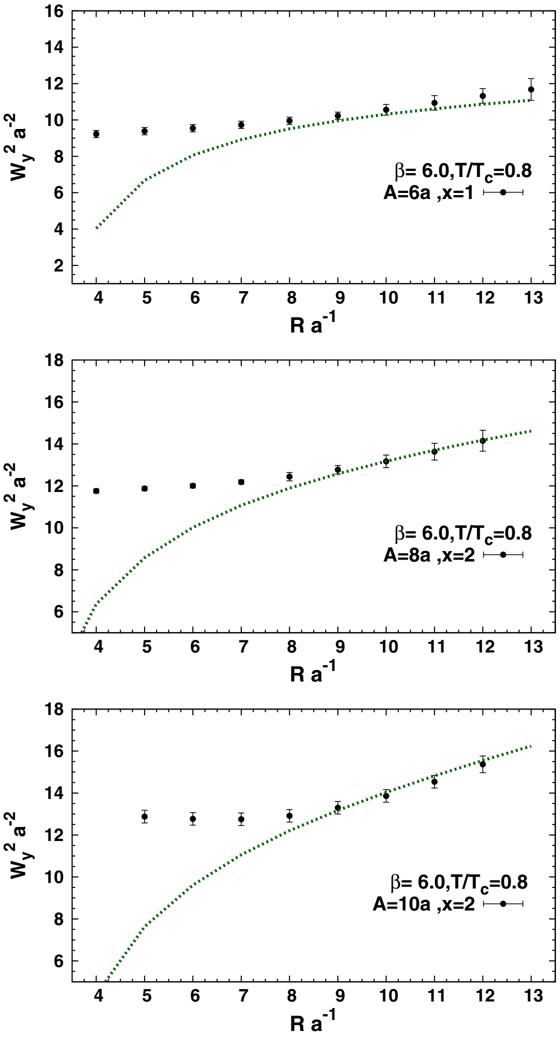

FIG. 17 (color online). The in-plane width W_y^2 of the action density at temperature $T/T_c = 0.8$ for the depicted transverse plane and the indicated isosceles base A. The lines correspond to the width according to the best fits to the string picture formula of Eq. (19).

TABLE V. Same as Table IV; however the values of the χ^2_{dof} are returned from the fits of the formula in Eq. (16) to the perpendicular width of the action density W_z^2.

(a) $A = 6a$

Fit range	5–12	6–12	7–12	8–12	9–12	10–12
$\chi^2_{\mathrm{dof}}(1)$	1.6	1.8	1.7	1.5	1.3	0.5
$\chi^2_{\mathrm{dof}}(2)$	3.2	3.3	3.1	2.6	2.1	0.8
$\chi^2_{\mathrm{dof}}(3)$	6.2	6.4	5.8	5.0	4.0	1.5
$\chi^2_{\mathrm{dof}}(4)$	10.5	10.7	9.7	8.4	6.8	2.7

(b) $A = 8a$

Fit range	05–12	6–12	7–12	8–12	9–12	10–12
$\chi^2_{\mathrm{dof}}(1)$	9.7	1.6	0.7	0.9	1.1	0.8
$\chi^2_{\mathrm{dof}}(2)$	5.0	1.5	1.4	1.7	1.8	1.43
$\chi^2_{\mathrm{dof}}(3)$	9.2	5.6	6.6	9.7	8.5	6.1
$\chi^2_{\mathrm{dof}}(4)$	11.6	10.1	12.1	13.6	14.0	9.0

(c) $A = 10a$

Fit range	5–12	6–12	7–12	8–12	9–12	10–12
$\chi^2_{\mathrm{dof}}(1)$	85.1	22	3.6	1.6	1.0	0.4
$\chi^2_{\mathrm{dof}}(2)$	77.2	15.4	2.3	0.3	0.3	0.4
$\chi^2_{\mathrm{dof}}(3)$	74.2	16.0	3.0	1.0	1.4	1.4
$\chi^2_{\mathrm{dof}}(4)$	74.2	16.5	3.7	1.1	1.4	1.6

greatest contribution of the junction appears to be in one lattice spacing immediately before the plane at which the profile of the two Gaussians intersect $u(x_0) = 0$, i.e, $x_0 - 1$. We shall see in what follows a more clear manifestation of this observation for the analysis at the other temperature, $T/T_c = 0.9$.

Table V summarizes the returned χ^2_{dof} from the fits of the perpendicular fluctuations of Eq. (16) to the perpendicular mean-square width profile W_z^2 listed in Table X. Figure 18 plots the corresponding best fits to the string model at the depicted selected planes for each triangle base parameter.

The perpendicular fluctuations return good χ^2_{dof}' s for widths measured at the plane $x = 1$ and third source Q_3 separations commencing from $R > 6$ fm for $A = 6a$. Also similar to the in-plane fluctuations discussed above, good χ^2_{dof}' s are obtained for both the plane $x = 1$ and the plane $x = 2$ for the triangular configuration of base lengths $A = 8a$ and $A = 10a$. Figure 18 demonstrates that for the largest triangle bases the deviations from the string behavior manifest clearly for the width corresponding to third quark separations $R < 6$. In the case of the small base the two strings of the Y shape are more close in space and self-interactions can cause larger deviations to be observed.

At the highest temperature $T/T_c = 0.9$, inspection of Table VI shows in general a similar behavior with respect to the points at small Q_3 source separations with a high value of the returned χ^2_{dof} if the entire range, i.e., $R = 5a$ to $R = 12a$, is considered. $\chi^2_{\mathrm{dof}} = 1.1$ is returned for a third source Q_3 separation $R = 6$ fm for the isosceles configuration corresponding to base length $A = 6a$. This manifests at the plane $x = 2$ which is one plane immediately before the plane $x_0 = 3$ at which $u(x_0) = 0$, i.e, where the two Gaussians coincide as depicted in Fig. 9. This is also manifest for both of the other two triangular configurations of base length parameters $A = 8a$ and $A = 10a$ where the best values of χ^2_{dof} (around 1) are obtained at the plane $x = 3$ and $x = 4$, respectively. In comparison with the fit behavior at the other temperature $T/T_c = 0.8$, this shows that the best fits change in accord with the change in the position of the intersection point $u(x_0) = 0$ at which the two Gaussians coincide. Figure. 19 shows the behaviour of χ^2_{dof} at the corresponding planes for the highest temperature $T/T_c = 0.9$. In Figs. 20 and 21 we plot the corresponding best fits of the string model with the in-plane and perpendicular action density, respectively.

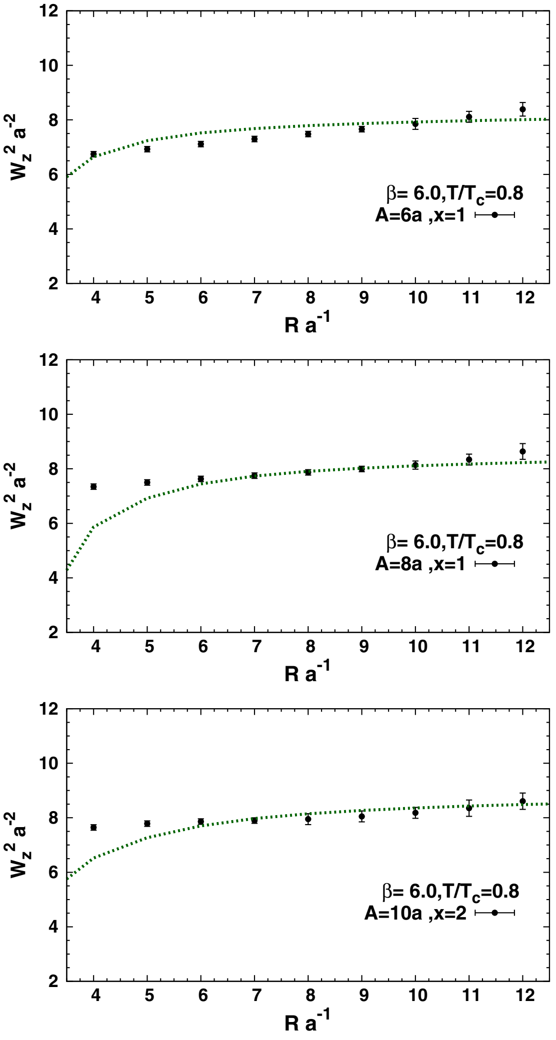

FIG. 18 (color online). The perpendicular width W_z^2 at temperature $T/T_c = 0.8$ for the depicted transverse planes, x, and the isosceles base of the corresponding triangular quark arrangement. The lines correspond to the best fits of the string model formula in Eq. (16).

The fits to the two-Gaussian profile and fits to the width of the string fluctuations are two independent sets of profile functions, even though both seem to behave in accord with each other in regard to the change in the position of the plane returning the best fits, $x_0 - 1$, and that at which the two Gaussians coincide, x_0. This suggests the physical realization that the two-Gaussian profiles (Figs. 8 and 9) are a manifestation of the average position due to the fluctuations of the underlying string structure and this point can be conceived as in favor of the Y-string picture.

For completeness, values of χ^2_{dof} in Table VII have been listed to show the returned fit parameters for the perpendicular fluctuations in Eq. (16). Figure VII shows the pattern of width increase at some of the planes returning best fits. These are in general less than its counterpart listed in Table VI for the in-plane width, even though we still

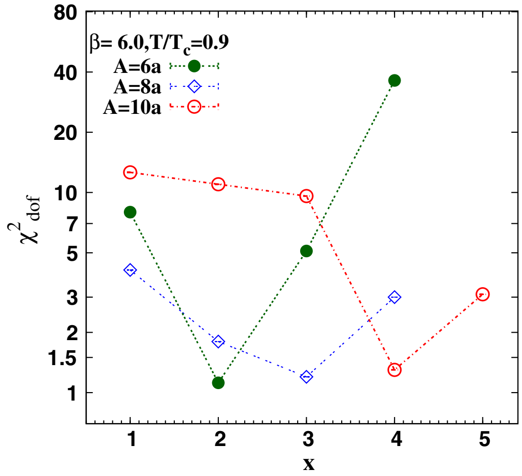

FIG. 19 (color online). The returned values of the χ^2_{dof} for the isosceles base $A = 0.6a$, $A = 0.8a$, and $A = 1.0a$. The plotted values correspond to the fits of the in-plane width of the action density to string model formula equation (19) at $T/T_c = 0.9$.

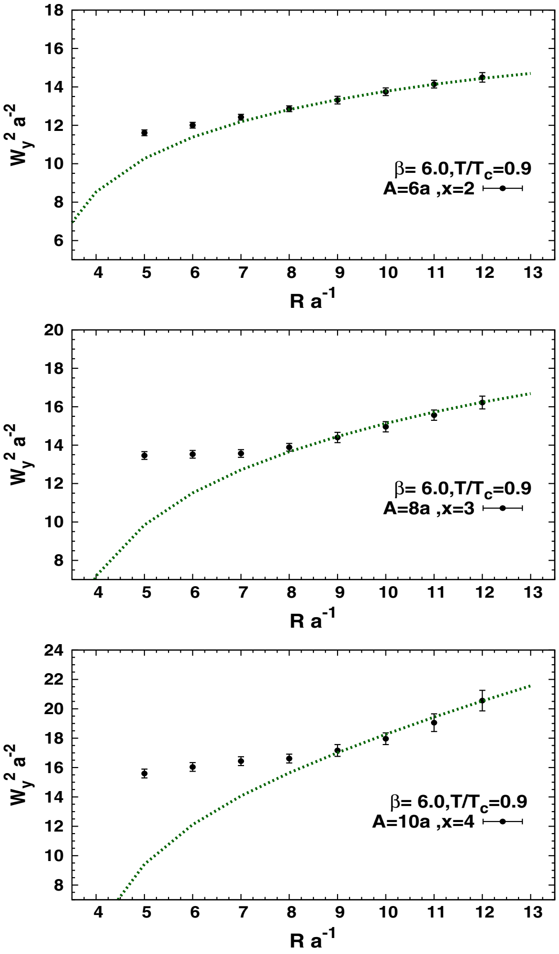

FIG. 20 (color online). Similar to Fig. 17 for the width of the in-plane action density W_y^2 at temperature $T/T_c = 0.9$ for the depicted transverse planes, x.

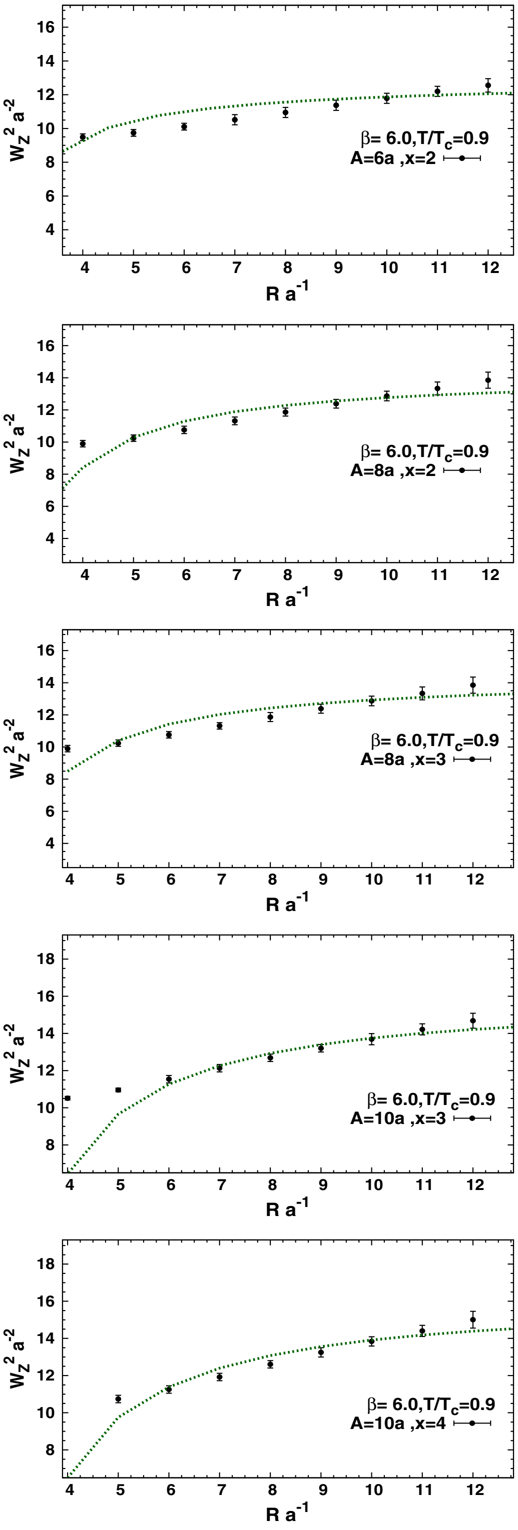

FIG. 21 (color online). Similar to Fig. 18 for the width of the perpendicular component of the action density W_z^2 at temperature $T/T_c = 0.9$.

obtain the best fits at the same planes obtained for the in-plane action density width.

A general theme of fits discussed above is that, with the points at short distances excluded from the fit, the returned χ^2_{dof} is smaller. The Y-string picture at finite temperature poorly describes the lattice data at short distances. The plots depict that the fluctuations of the junction of the Y-free string have a more suppressed profile than the flux tube observed in lattice gauge theory at short distances. Inspection of Fig. 11 shows that the Gaussian-like flux tubes describe a configuration that resembles a Δ shape or in more precise terms the junction either coincides or is very close to the third quark at short distances $R = 3a, 4a, 5a$. On the other hand, the growth of the flux tube diameter, which matches with the predictions of the string model, seems to manifest at large source separation where the length of the third string is large enough to reduce the effects of the self-interaction of the third quark Q_3 with the junction. This also is consistent with the fact that the effective string is a working picture at large source distances [4,9,14,19–22,53,63,64].

TABLE VI. The returned values of the $\chi^2_{\mathrm{dof}}(x)$ corresponding to fits of the in-plane width $W_y^2(x)$ of the action density at each plane x to the string model formula equation (16). The fits are for isosceles triangle quark configurations of base $A = 6a$, $A = 8a$, and $A = 10a$ at $T/T_c = 0.9$.

(a) $A = 6a$

Fit range	5–9	5–10	5–11	5–12	6–12	7–12	8–12
$\chi^2_{\mathrm{dof}}(1)$	31.76	43.24	46.2	7.79	7.97	3.42	0.42
$\chi^2_{\mathrm{dof}}(2)$	1.37	1.29	1.12	0.96	1.12	0.17	0.12
$\chi^2_{\mathrm{dof}}(3)$	10.6	9.72	8.6	8.02	5.06	4.4	1.02
$\chi^2_{\mathrm{dof}}(4)$	50	43.5	38.16	34.4	36.3	7.8	2.6

(b) $A = 8a$

Fit range	5–9	5–10	7–11	5–12	6–12	7–12	8–12
$\chi^2_{\mathrm{dof}}(1)$	49.9	26.5	3.4	67.8	19.8	4.0	1.4
$\chi^2_{\mathrm{dof}}(2)$	18.6	23.3	1.7	56.2	7.8	1.8	0.4
$\chi^2_{\mathrm{dof}}(3)$	5.13	22.6	1.0	52.3	21	1.2	0.6
$\chi^2_{\mathrm{dof}}(4)$	89	111	25.2	128	60	30	16

(c) $A = 10a$

Fit range	5–9	7–9	7–11	6–12	7–12	8–12	9–12
$\chi^2_{\mathrm{dof}}(1)$	167	34.7	40.3	94.8	51	12.67	6.18
$\chi^2_{\mathrm{dof}}(2)$	286.2	38	31.5	74.7	29	11	3.96
$\chi^2_{\mathrm{dof}}(3)$	116.5	80	51.9	73	43.2	9.6	1.02
$\chi^2_{\mathrm{dof}}(4)$	63.5	7.7	5.4	38.5	3.5	1.3	0.2
$\chi^2_{\mathrm{dof}}(5)$		10.5	7.2	5.6	6.3	3.1	0.9

From the above discussion, we conclude that the Y-string picture with a minimal length of the string entails a mean-square width of its quantum fluctuations which is consistent with the lattice gauge data at large color-source separation. The Y-string configurations provide good fits for planar triangular quark configurations with minimal height length $0.7 \leq R \leq 1.3$ fm and bases $0.6 \leq A \leq 1.0$ fm for both the in-plane and off-plane width profile. This result shows that

TABLE VII. Similar to Table VI: the returned values of the $\chi^2_{\rm dof}$ corresponds to the width in the perpendicular plane W_z^2. Fits of the action density to string model formula in Eq. (16) at each depicted plane.

(a) $A = 6a$

Fit range	5–12	6–12	7–12	8–12	9–12	10–12
$\chi^2_{\rm dof}(1)$	1.4	1.6	1.5	1.3	1.1	0.8
$\chi^2_{\rm dof}(2)$	2.5	2.6	1.8	1.3	1.0	0.6
$\chi^2_{\rm dof}(3)$	5.7	5.6	4.6	3.4	2.3	1.4
$\chi^2_{\rm dof}(4)$	9.3	9.2	7.5	5.3	3.4	1.9

(b) $A = 8a$

Fit range	5–12	6–12	7–12	8–12	9–12	10–12
$\chi^2_{\rm dof}(1)$	2.1	1.2	1.4	1.4	1.5	1.3
$\chi^2_{\rm dof}(2)$	1.4	1.2	1.4	1.3	1.0	0.9
$\chi^2_{\rm dof}(3)$	1.6	1.7	1.8	1.5	1.1	0.7
$\chi^2_{\rm dof}(4)$	3.7	4.4	4.0	3.0	1.9	1.0

(c) $A = 10a$

Fit range	5–12	6–12	7–12	8–12	9–12	10–12
$\chi^2_{\rm dof}(1)$	14.3	2.2	1.5	1.9	2.3	2.4
$\chi^2_{\rm dof}(2)$	5.7	1.4	0.9	1.2	1.4	1.5
$\chi^2_{\rm dof}(3)$	4.5	1.0	0.94	1.14	1.2	1.1
$\chi^2_{\rm dof}(4)$	2.7	1.1	1.3	1.2	1.0	0.7

the stringlike behavior manifests in the baryonic configurations at large quark separations.

V. SUMMARY AND PROSPECTIVE

In this paper we have discussed the baryonic stringlike behavior in the profile of the gluonic flux of a three-quark system in pure SU(3) Yang-Mills vacuum at finite temperature. The gluon flux is measured as a correlation between the action density operator and three traced (gauge-invariant) Polyakov lines. Measurements of the mean-square width have been taken near the end of QCD phase diagram $T/T_c = 0.8$ and just before the deconfinement point $T/T_c = 0.9$.

For noise reduction, an average over the configuration space has been calculated for over 500 independent bins. In each bin an average of over 20 measurements has been calculated in addition to an average over space-time symmetries. The two lattices analyzed here are cooled with a stout-link smoothing algorithm with a number of sweeps such that the physics of focus is preserved in a systematic and controlled manner [53,76].

The Y-baryonic string model has been discussed at high temperature for the width profile of the junction. The leading order solution presented in Ref. [30] has been considered here. The thermal effects, however, have been incorporated into the formulas accounting for the mean-square width of the string's junction.

We have shown a qualitative description of the rendered action density profile in the context of the consistency with the stringlike behavior. The qualitative feature of these density plots at large source separation does not seem to indicate an action density pattern resembling the shape of tubes that would form around the perimeter of the three quarks. The distribution is a "filled" Δ and displays a peak close to the geometrical center of the triangle. In addition, the transverse profile of the action density fits to a double Gaussian function. The profile of the double Gaussian describes a clear Y-shaped system of Gaussian flux tubes. The revealed configurations of these Gaussian flux tubes is dynamic and reconfigures in accord with the quark configuration and temperature. The total length of the three Gaussian flux tubes is maximal for the temperature just before the deconfinement point. However, the length approaches the geometrical minimal length at the temperature near the end of the QCD plateau $T/T_c = 0.8$. The flux density shows an asymmetric width profile between that in the plane of the three quark and that in the perpendicular direction which indicates a greater restoring force in the quarks' plane.

The lattice data for the mean-square width of the gluonic action density has been compared to the corresponding width based on string model at finite temperature. We have revealed the characteristics of the growth pattern of the gluonic action density for three sets of geometrical three-quark configurations with respect to fits to the Y-string model. The planes close to the junction in the profile of the double Gaussian return good fits to the width of the junction fluctuations in baryonic string model only for large quark separation for both the considered temperatures.

The analysis presented here is of particular relevance to the confining string models, since reports on effects of bosonic strings are usually discussed on the level of the mesonic flux tubes. Apart from the simulations first presented on the Y-string effects of the 3-Potts model [29,37], it is our first examination of the effects of the Y-bosonic strings in the action density of the quenched QCD, to the best of our knowledge.

The stringlike behavior of the confining flux tubes at the two temperature scales enabled increased insight into the dynamics of the profile with the temperature changes. It would be insightful as well to examine the parametrization ansatz [42,43,77] of the confining potential, where the effects of the junction could give rise to different behavior at both temperatures. We report this separately elsewhere. In addition, we study the limiting case of the diquark-quark systems [78] and set out the relevant distance scale where the properties of the mesonic string unambiguously manifest.

In light of the present discussion which focused on revealing the Y-string aspects of the Δ-shaped action density manifesting in the baryon at finite temperature

[27,28], in addition to the recent observation that the string tension is indicating a quite flat QCD plateau [79] near the lowest temperature $T/T_c = 0.8$ considered here. These strongly pose that the revealed color map in baryons at the temperatures considered here could be a potential form for the exact geometry of the flux tube arrangements in the baryon, if the analysis with Polyakov loops is extended to the low temperature regime of pure SU(3) Yang-Mills theory. In addition, it would be interesting to extend the above analysis to reveal the Y-string effects at low temperatures.

We suggest a consistent inclusion of an UV-filtering step into the updating cycles of the Lüscher-Weiss (LW) multilevel algorithm to probe the energy distribution of static baryons in the low temperature regimes of the quenched theory [80]. This technique is expected to contribute to the efficiency of the LW algorithm and to reduce the computational time to extend the present analysis to lower temperatures, which is the goal of our next project.

ACKNOWLEDGMENTS

We would like to thank Philippe de Forcrand, Ohta Shigemi, Hideo Suganuma, and Dmitriy Zanin for the useful comments and discussions. The authors thank the Yukawa Institute for Theoretical Physics, Kyoto University. Discussions during the YITP workshop YITP-T-14-03 on “Hadrons and Hadron Interactions in QCD" were useful in completing this work. This work has been funded by the Chinese Academy of Sciences president’s international fellowship initiative, Grant No. 2015PM062, NSFC Grants (No. 11035006, No. 11175215, No. 11175220), and the Hundred Talents Program of the Chinese Academy of Sciences (Y101020BR0).

APPENDIX A: STRING PARTITION FUNCTION

We calculate the string’s thickness at the junction position. In the following, we follow the same procedures of the calculations presented in Refs. [29,30] however, taking into account a convoluted fluctuations $\phi \to \int_{-\infty}^{\infty} \phi(\tau)\psi(t-\tau)d\tau$ to incorporate thermal effects with the fluctuations as discussed in Sec. II.

The calculation of the corresponding partition function in Eq. (9) requires evaluating the integral over the minimal area swept due to perpendicular fluctuations ϕ, and the determinant of the Laplacian.

Conformally mapping the string’s blade a to a rectangle [29], see Fig. 22,

$$f_i(z) = z + \frac{1}{\sqrt{T}}\sum_{w\neq 0}\frac{\eta_i\cdot\phi_w\psi(wL_i)}{\sinh(wL_i)}e^{wz}. \tag{A1}$$

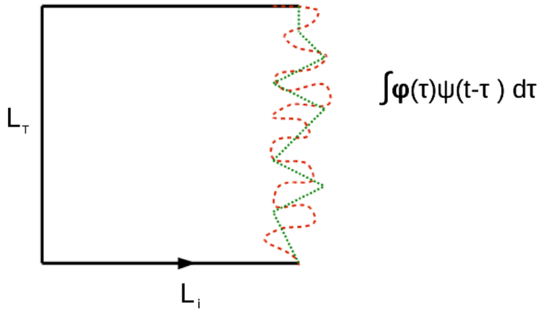

FIG. 22 (color online). The domain Θ_i is conformally mapped onto a rectangle $L_i' \times L_T$, the first order fluctuations are convoluted with a smoothing scalar ψ.

The minimal-area solution for a fixed junction configuration

$$\xi_{\min,i} = \frac{1}{\sqrt{T}}\sum_w \phi_{w,zi}\psi_w \frac{\sinh(ws)}{\sinh(wL_i)}e^{iwt}, \tag{A2}$$

taking into account that the minimal-area solution for a fixed position of the junction, $\xi_{\min,i}(t,s)$, is harmonic and satisfies the boundary conditions

$$\Delta\xi_{\min,i} = 0, \xi_{\min,i}(t, L_i + \eta_i\cdot\phi(t)) = \phi_{zi}(t). \tag{A3}$$

The integral in Eq. (9) would then read

$$\begin{aligned}\int_{\Theta_i} d^2\zeta \sum_i \frac{\partial\xi_{\min,i}}{\partial}\zeta_i\cdot\frac{\partial\xi_{\min,i}}{\partial}\zeta_i \\ = \sum_w w\coth(wL_i)|\phi_{w,zi}|^2\psi_w^2.\end{aligned} \tag{A4}$$

The determinant in Eq. (9) is obtained by mapping the domain Θ_i conformally to a rectangle $L_i' \times L_T$, taking into account the change in the Laplacian [12,30]. Using the above conformal map equation (A1), we obtain to leading order

$$\ln\frac{\det(-\Delta_\Theta)}{\det(-\Delta_{\tilde{\Theta}})} = \frac{1}{12\pi}\sum_w w^3|\eta_i\cdot\phi_w|^2\coth(wL_i)\psi(w). \tag{A5}$$

Further conformally mapping the above into a circle and making use of (A5), the determinant of the Laplacian with respect to the blade a would then read

$$\begin{aligned}\det(-\Delta_{\Theta_i}) = \eta^2\left(\frac{iL_T}{2L_i'}\right) \\ \times\exp\left(-\frac{1}{12\pi}\sum_w w^3\coth(wL_i)|\eta_i\cdot\phi_w|^2\psi_w^2\right),\end{aligned} \tag{A6}$$

where $\eta(\tau)$ is the Dedekind function.

APPENDIX B: THE JUNCTION’S WIDTH

The thickness of the string at the junction can be calculated [30] taking the expectation value of ϕ^2,

$$\langle \phi^2 \rangle = \frac{\int D\phi \phi^2 \psi_w^2 e^{-S}}{\int D\phi e^{-S}}. \tag{B1}$$

The above second moment of the junction can be decomposed into perpendicular z and parallel (in-plane) xy fluctuations,

$$\langle \phi^2 \rangle = \langle {\phi_z}^2 \rangle + \langle {\phi_{xy}}^2 \rangle = \frac{I_{z,2}}{I_{z,0}} + \frac{I_{xy,2}}{I_{xy,0}}, \tag{B2}$$

where

$$I_{z,2} = \int D\phi_z \phi_z^2 \exp\left\{ -\frac{1}{2} \sum_w \left[mw^2 + \sigma w \sum_a \coth(wL_a) \right] \times |\phi_{w,z}|^2 \right\}, \tag{B3}$$

$$\begin{aligned} I_{xy,2} = \int D\phi \phi^2 \exp\Bigg\{ \sum_w \Bigg[-\frac{1}{2}\left(mw^2 + \sigma w \sum_i \coth(wL_i) \right) \\ \times |\phi_w|^2 + |\phi_{w,x}|^2 Q_x + |\phi_{w,y}|^2 Q_y + |\phi_{w,y}|^2 Q_y \\ + 2((\phi_{w,x} . \phi_{w,y})) Q_{\mathrm{xy}} \Bigg] \Bigg\}, \end{aligned} \tag{B4}$$

with Q_x, Q_y, and Q_{xy} defined as in Eq. (21). Orthogonalizing the fluctuations for parallel fluctuations the above moments would then read

$$I_{x,2} = \int D\phi_x \phi_x^2 \exp\left\{ \sum_w \left[-\frac{1}{2}(F(w) + G_x(w)) \right] |\phi_{w,x}|^2 \right\},$$

$$I_{y,2} = \int D\phi_y \phi_y^2 \exp\left\{ \sum_w \left[-\frac{1}{2}(F(w) + G_y(w)) \right] |\phi_{w,y}|^2 \right\},$$

$$I_{z,2} = \int D\phi_z \phi_z^2 \exp\left\{ -\frac{1}{2} \sum_w R(w) |\phi_{w,z}|^2 \right\}.$$

$F(w)$, $G(w)$ and $R(w)$ are defined as

$$\begin{aligned} F(w) &= Q_{x,w} + Q_{y,w}, \\ G(w) &= (Q_{xy,w}^2 + (Q_{x,w} - Q_{y,w})^2)^{1/2}, \\ R(w) &= mw^2 + \sigma w \sum_i \coth(wL_i) \psi(w, L_i). \end{aligned} \tag{B5}$$

Solving for the above Gaussian integrals,

$$\begin{aligned} \langle \phi_x^2 \rangle &= \frac{I_{x,2}}{I_{x,0}} = \frac{2}{L_T} \sum_{w>0} \frac{1}{F(w) - G(w)}, \\ \langle \phi_y^2 \rangle &= \frac{I_{y,2}}{I_{y,0}} = \frac{2}{L_T} \sum_{w>0} \frac{1}{F(w) + G(w)}, \\ \langle \phi_z^2 \rangle &= \frac{I_{z,2}}{I_{z,0}} = \frac{2}{L_T} \sum_{w>0} \frac{1}{R(w)}, \end{aligned} \tag{B6}$$

with $w = 2\pi n / L_T$.

APPENDIX C

TABLE VIII. The width of the flux tube $W_y^2(x)$ at each consecutive transverse plane x_i from the quarks forming the base, A, of the isosceles triangle. The measurements for base source separation distance $A = 6a$ for the temperature $T/T_c = 0.8$ are indicated as a function of the third quark position, Q_3.

Plane $Q_3 = R/a$	$x = 1$	$x = 2$	$x = 3$	$x = 4$	$x = 5$	$x = 6$	$x = 7$	$x = 8$	$x = 9$	$x = 10$	$x = 12$
$A = 0.6$ fm											
7	9.7(1)	9.6(0)	9.3(0)	9.0(1)	8.6(1)	8.2(1)					
8	10.0(1)	9.9(1)	9.7(1)	9.5(1)	9.2(1)	8.7(1)	8.2(1)				
9	10.2(1)	10.3(1)	10.2(1)	10.0(1)	9.7(2)	9.3(2)	8.8(2)	8.2(1)			
10	10.6(1)	10.8(2)	10.6(2)	10.5(2)	10.3(2)	9.9(2)	9.4(2)	8.8(2)	8.0(1)		
11	10.9(2)	11.5(3)	11.2(3)	11.1(3)	10.9(3)	10.6(3)	10.2(2)	9.5(2)	8.6(1)	7.8(1)	
12	11.3(2)	12.5(5)	12.1(4)	11.8(4)	11.6(4)	11.3(4)	11.0(3)	10.3(2)	9.4(2)	8.4(2)	7.7(1)
13	11.7(3)	13.9(7)	13.2(6)	12.7(6)	12.4(6)	12.3(6)	12.1(5)	11.5(3)	10.4(2)	9.2(2)	8.3(2)
$A = 0.8$ fm											
7	11.3(4)	11.2(4)	11.3(1)	10.8(1)	10.2(1)	9.5(2)					
8	11.5(4)	11.4(4)	11.7(1)	11.2(1)	10.6(1)	10.0(2)	9.2(2)				
9	11.9(4)	11.6(4)	11.7(4)	11.6(1)	11.1(2)	10.5(2)	9.7(2)	8.8(2)			
10	12.4(5)	12.1(4)	11.8(2)	11.9(2)	11.4(2)	10.9(2)	10.2(2)	9.3(2)	8.2(2)		
11	13.1(5)	12.5(5)	12.1(2)	12.1(2)	11.5(2)	11.0(2)	10.4(1)	9.6(2)	8.5(3)	7.5(3)	
12	13.8(5)	13.0(5)	12.4(2)	12.1(2)	11.3(2)	10.8(2)	10.3(1)	9.6(2)	8.6(4)	7.6(4)	6.8(4)
$A = 1.0$ fm											
7	13.4(2)	12.7(2)	13.7(1)	12.9(0)	12.2(1)	11.4(2)					
8	13.6(2)	12.9(2)	13.8(2)	13.0(1)	12.3(0)	11.5(1)	10.6(2)				
9	14.0(3)	13.3(2)	13.7(3)	12.9(2)	12.1(1)	11.5(1)	10.6(2)	9.5(2)			
10	14.5(4)	13.8(4)	13.3(4)	11.7(2)	11.0(2)	10.4(2)	9.4(3)	8.1(4)			
11	15.0(5)	14.5(6)	13.9(3)	10.9(4)	10.2(4)	9.6(5)	9.0(6)	7.9(6)	6.6(6)		
12	15.5(7)	15.4(8)	14.8(6)	9.7(7)	8.9(7)	8.3(8)	7.8(9)	7(1)	6(1)	5(1)	5(1)

TABLE IX. Same as Table VIII; however the width measurements are taken at the temperature $T/T_c = 0.9$.

Plane $Q_3 = R/a$	$x = 1$	$x = 2$	$x = 3$	$x = 4$	$x = 5$	$x = 6$	$x = 7$	$x = 8$	$x = 9$	$x = 10$	$x = 12$
$A = 0.6$ fm											
7	12.9(2)	12.4(2)	12.5(0)	12.0(1)	11.4(2)	10.9(3)					
8	13.5(1)	12.9(3)	12.9(0)	12.6(1)	12.1(1)	11.4(2)	10.7(3)				
9	13.6(6)	13.3(2)	13.2(0)	13.0(0)	12.7(1)	12.1(2)	11.4(2)	10.6(3)			
10	13.9(3)	13.6(1)	13.4(1)	13.4(0)	13.2(0)	12.8(1)	12.2(2)	11.3(2)	10.5(3)		
11	14.1(2)	14.1(2)	14.2(6)	13.6(1)	13.6(1)	13.4(1)	13.0(1)	12.2(2)	11.2(2)	10.2(3)	
12	14.3(2)	14.5(6)	14.7(2)	13.7(2)	13.9(2)	13.9(1)	13.7(1)	13.1(1)	12.1(2)	10.9(2)	9.8(2)
$A = 0.8$ fm											
7	13.2(1)	13.3(2)	13.6(1)	13.5(3)	13.3(2)	12.4(3)					
8	13.5(1)	13.7(2)	13.9(3)	14.5(0)	14.0(1)	13.0(2)	12.0(3)				
9	13.9(1)	14.1(2)	14.4(3)	15.4(1)	14.7(0)	13.8(1)	12.7(2)	11.7(3)			
10	14.1(2)	14.5(3)	15.0(4)	15.8(2)	15.4(1)	14.7(1)	13.7(2)	12.5(2)	11.3(3)		
11	14.4(2)	14.9(4)	15.6(4)	16.2(3)	15.9(2)	15.5(1)	14.7(1)	13.5(2)	12.2(3)	10.9(3)	
12	14.6(2)	15.3(5)	16.2(7)	(5)	16.5(3)	16.2(2)	15.7(2)	14.7(2)	13.4(2)	11.8(2)	10.5(4)
$A = 1.0$ fm											
7	17.1(2)	16.7(2)	16.3 (1)	16.4(5)	15.9(1)	14.5(3)					
8	17.6(3)	17.2(2)	16.7 (1)	16.6(2)	16.7(0)	15.2(2)	13.8(3)				
9	18.0(3)	17.7(2)	17.4 (2)	17.1(3)	17.5(1)	16.1(1)	14.5(2)	13.0(3)			
10	18.5(4)	18.3(3)	18.1 (4)	17.9(5)	18.3(2)	17.1(1)	15.6(1)	13.9(2)	12.4(3)		
11	19.0(4)	19.0(5)	19.0 (6)	19.1(5)	19.1(4)	18.1(2)	16.8(1)	15.1(2)	13.4(3)	11.7(3)	
12	19.3(5)	19.7(6)	20 (6)	20.6(7)	20.1(5)	19.2(4)	18.1(3)	16.5(2)	14.7(2)	12.8(3)	11.2(4)

TABLE X. The width of the perpendicular width of the flux tube to the 3Q plane at each consecutive transverse plane x_i from the quarks forming the base, A, of the isosceles triangle. The measurements are taken at the temperature $T/T_c = 0.8$.

Plane $Q_3 = R/a$	$x = 1$	$x = 2$	$x = 3$	$x = 4$	$x = 5$	$x = 6$	$x = 7$	$x = 8$	$x = 9$	$x = 10$	$x = 11$
$A = 0.6$ fm											
4	6.7(1)	6.7(1)	6.7(1)								
5	6.9(1)	6.9(1)	6.9(1)	6.8(1)							
6	7.1(1)	7.1(1)	7.1(1)	7.1(1)	7.0(1)						
7	7.3(1)	7.3(1)	7.4(0)	7.4(1)	7.3(1)	7.2(1)					
8	7.5(1)	7.6(1)	7.7(1)	7.7(0)	7.6(1)	7.5(1)	7.4(1)				
9	7.7(1)	7.8(1)	7.9(1)	8.0(1)	8.0(1)	7.9(1)	7.8(1)	7.8(2)			
10	7.9(1)	8.0(1)	8.3(1)	8.4(1)	8.5(1)	8.5(1)	8.4(1)	8.4(2)	8.5(2)		
11	8.1(1)	8.4(1)	8.7(1)	9.0(1)	9.1(1)	9.1(1)	9.1(2)	9.2(2)	9.3(2)	9.5(4)	
12	8.5(2)	8.9(2)	9.3(2)	9.7(2)	10.0(2)	10.1(2)	10.1(2)	10.2(2)	10.4(4)	10.6(4)	10.7(5)
$A = 0.8$ fm											
4	7.3(1)	7.2(1)	7.2(1)								
5	7.5(1)	7.4(1)	7.3(1)	7.3(1)							
6	7.6(1)	7.5(1)	7.5(1)	7.4(1)	7.3(1)						
7	7.7(1)	7.7(1)	7.6(1)	7.6(1)	7.5(1)	7.4(1)					
8	7.9(1)	7.8(1)	7.8(1)	7.8(1)	7.8(1)	7.7(2)	7.6(2)				
9	8.0(1)	8.0(1)	8.0(1)	8.0(1)	8.0(2)	8.0(2)	8.0(2)	8.1(4)			
10	8.1(2)	8.2(2)	8.2(2)	8.3(2)	8.3(2)	8.4(2)	8.5(2)	8.7(5)	9.1(5)		
11	8.3(2)	8.4(2)	8.6(2)	8.7(2)	8.8(2)	8.9(2)	9.2(5)	9.6(5)	10.0(8)	10.3(7)	
12	8.6(4)	8.9(4)	9.2(2)	9.4(2)	9.6(2)	9.8(5)	10.1(6)	10.7(9)	11.3(7)	11.6(9)	11.4(9)
$A = 1.0$ fm											
4	7.8(1)	7.6(1)	7.5(1)								
5	8.0(1)	7.8(1)	7.6(1)	7.6(1)							
6	8.1(1)	7.9(1)	7.7(1)	7.6(1)	7.5(2)						
7	8.1(2)	7.9(1)	7.7(1)	7.7(1)	7.6(2)	7.5(2)					
8	8.2(2)	8.0(2)	7.7(2)	7.6(2)	7.6(2)	7.5(2)	7.5(4)				
9	8.3(2)	8.0(2)	7.8(2)	7.7(2)	7.6(2)	7.6(4)	7.6(4)	7.8(5)			
10	8.3(2)	8.2(2)	8.0(4)	7.8(4)	7.7(4)	7.7(5)	7.9(5)	8.3(6)	8.7(5)		
11	8.2(5)	8.4(5)	8.2(5)	8.0(5)	7.9(5)	7.9(5)	8.3(8)	8.9(9)	9.5(6)	9.7(4)	
12	8.2(8)	8.6(6)	8.7(5)	8.5(5)	8.3(5)	8.4(8)	8.8(8)	9.6(9)	10.5(7)	10.7(4)	10.3(4)

TABLE XI. The percentage difference e between the in-plane width measurements $(W_y^{(1)}(x))^2$ with a single Gaussian form [28] relative to the width measured using a two-Gaussian form $(W_y^{(2)}(x))^2$ calculated as $e = |((W_y^{(1)}(x))^2 - (W_y^{(2)}(x))^2)/(W_y^{(2)}(x))^2|$, at temperature $T/T_c = 0.8$, and for the selected quark configurations.

Plane $Q_3 = R/a$	$R = 5$	$R = 7$	$R = 9$	$R = 11$
$A = 0.8$ fm				
$x = 1$	8%	7%	7%	4%
$x = 2$	5%	6%	9%	9%
$A = 1.0$ fm				
$x = 1$	15.0%	10%	8.2%	13.2%
$x = 2$	15.0%	9%	2.7%	13.2%

TABLE XII. Same as Table X; however the perpendicular width of the action density $W_z^2(x)$ has been measured at the temperature $T/T_c = 0.9$.

Plane $Q_3 = R/a$	$x = 1$	$x = 2$	$x = 3$	$x = 4$	$x = 5$	$x = 6$	$x = 7$	$x = 8$	$x = 9$	$x = 10$	$x = 11$
$A = 0.6$ fm											
4	9.5(2)	9.5(2)	9.5(2)								
5	9.7(2)	9.7(2)	9.7(2)	9.7(2)							
6	10.0(2)	10.1(2)	10.2(2)	10.1(2)	9.9(2)						
7	10.3(2)	10.5(2)	10.7(2)	10.6(2)	10.4(2)	10.2(2)					
8	10.7(2)	10.9(2)	11.2(2)	11.3(2)	11.2(2)	10.9(2)	10.6(4)				
9	11.0(2)	11.4(2)	11.7(2)	11.9(2)	11.9(2)	11.7(2)	11.3(4)	11.0(4)			
10	11.4(2)	11.8(2)	12.2(2)	12.5(2)	12.6(2)	12.6(2)	12.2(2)	11.8(4)	11.3(4)		
11	11.8(4)	12.2(2)	12.7(2)	13.1(2)	13.3(2)	13.4(2)	13.2(4)	12.8(4)	12.3(4)	11.8(5)	
12	12.3(4)	12.7(4)	13.1(2)	13.6(2)	14.0(2)	14.2(4)	14.3(4)	14.0(4)	13.5(5)	12.9(5)	12.5(5)
$A = 0.8$ fm											
4	10.1(2)	10.0(2)	9.9(2)								
5	10.5(2)	10.4(2)	10.2(2)	10.1(2)							
6	10.8(2)	10.8(2)	10.8(2)	10.6(2)	10.4(2)						
7	11.2(2)	11.3(2)	11.3(2)	11.2(2)	11.0(2)	10.7(4)					
8	11.5(2)	11.7(2)	11.9(2)	11.9(2)	11.7(2)	11.4(4)	11.1(4)				
9	11.9(2)	12.1(2)	12.4(2)	12.5(2)	12.5(2)	12.2(2)	11.8(4)	11.4(4)			
10	12.3(2)	12.6(2)	12.9(2)	13.1(2)	13.2(2)	13.1(2)	12.7(4)	12.2(4)	11.8(5)		
11	12.8(4)	13.0(2)	13.3(2)	13.6(2)	13.9(2)	13.9(2)	13.7(4)	13.2(4)	12.7(5)	12.3(5)	
12	13.4(4)	13.6(4)	13.8(2)	14.2(2)	14.5(2)	14.7(4)	14.7(4)	14.3(5)	13.8(5)	13.3(5)	13.1(5)
$A = 1.0$ fm											
4	11.0(2)	10.7(2)	10.5(2)								
5	11.4(2)	11.2(2)	11.0(2)	10.7(2)							
6	11.8(2)	11.7(2)	11.5(2)	11.3(2)	11.0(4)						
7	12.2(2)	12.2(2)	12.1(2)	11.9(2)	11.6(4)	11.3(4)					
8	12.6(2)	12.6(2)	12.7(2)	12.6(2)	12.4(4)	12.0(4)	11.7(5)				
9	13.0(2)	13.1(2)	13.2(2)	13.2(2)	13.1(2)	12.8(4)	12.4(4)	12.0(5)			
10	13.4(2)	13.5(2)	13.7(2)	13.8(2)	13.9(2)	13.7(4)	13.3(4)	12.8(5)	12.4(5)		
11	14.1(2)	14.1(2)	14.2(2)	14.4(2)	14.6(2)	14.6(4)	14.3(4)	13.8(5)	13.2(5)	13.0(5)	
12	15.0(4)	14.9(2)	14.9(2)	15.0(2)	15.2(2)	15.4(4)	15.3(5)	14.8(5)	14.3(5)	13.9(6)	13.9(8)

TABLE XIII. Same as Table XI; however the percentage difference has been calculated for in-plane width at the temperature $T/T_c = 0.9$.

Plane $Q_3 = R/a$	$R = 5$	$R = 7$	$R = 9$	$R = 11$
$A = 0.6$ fm				
$x = 1$	2.3%	2.0%	1.0%	3.0%
$x = 2$	5.1%	3.2%	0.1%	5.0%
$A = 0.8$ fm				
$x = 1$	25.2%	25.7%	24.4%	28.4%
$x = 2$	18.9%	18.9%	15.6%	12.0%
$x = 3$	4.4%	11.0%	10.4%	5.1%
$A = 1.0$ fm				
$x = 1$	24.8%	25.1%	22.2%	23%
$x = 2$	19.2%	20.3%	16.9%	15.7%
$x = 3$	9.0%	15.3%	13.2%	5%
$x = 4$	1.0%	6.0%	5.8%	4%

[1] K. G. Wilson, Phys. Rev. D **10**, 2445 (1974).

[2] G. Parisi, Phys. Rev. D **11**, 970 (1975).

[3] S. Mandelstam, Phys. Rep. **23**, 245 (1976).

[4] M. Luscher and P. Weisz, J. High Energy Phys. 07 (2002) 049.

[5] M. Creutz, Phys. Rev. D **21**, 2308 (1980).

[6] Y. Nambu, Phys. Lett. **80B**, 372 (1979).

[7] P. Olesen, Phys. Lett. **160B**, 144 (1985).

[8] J. Ambjorn, P. D. Forcrand, F. Koukiou, and D. Petritis, Phys. Lett. B **197**, 548 (1987).

[9] K. J. Juge, J. Kuti, and C. Morningstar, Phys. Rev. Lett. **90**, 161601 (2003).

[10] M. Caselle, M. Panero, P. Provero, and M. Hasenbusch, Nucl. Phys. B, Proc. Suppl. **119**, 499 (2003).

[11] F. Gliozzi, arXiv:hep-lat/9410022.

[12] M. Luscher, K. Symanzik, and P. Weisz, Nucl. Phys. **B173**, 365 (1980).

[13] G. 't Hooft, in *Proceedings of the EPS International Conference on High Energy Physics, Palermo, Italy, 1975*, p.1225.

[14] G. S. Bali, C. Schlichter, and K. Schilling, Phys. Rev. D **51**, 5165 (1995).

[15] Y. Peng and R. W. Haymaker, Phys. Rev. D **47**, 5104 (1993).

[16] S. Thurner, M. Feurstein, H. Markum, and W. Sakuler, Phys. Rev. D **54**, 3457 (1996).

[17] M. S. Cardaci, P. Cea, L. Cosmai, R. Falcone, and A. Papa, Phys. Rev. D **83**, 014502 (2011).

[18] M. Luscher, G. Munster, and P. Weisz, Nucl. Phys. **B180**, 1 (1981).

[19] P. Pennanen, A. M. Green, and C. Michael, Phys. Rev. D **56**, 3903 (1997).

[20] M. Caselle, F. Gliozzi, U. Magnea, and S. Vinti, Nucl. Phys. **B460**, 397 (1996).

[21] F. Gliozzi, M. Pepe, and U.-J. Wiese, Phys. Rev. Lett. **104**, 232001 (2010).

[22] F. Gliozzi, M. Pepe, and U.-J. Wiese, J. High Energy Phys. 01 (2011) 057.

[23] F. Okiharu and R. Woloshyn, Nucl. Phys. B, Proc. Suppl. **129–130**, 745 (2004).

[24] F. Bissey, F-G. Cao, A. Kitson, B. G. Lasscock, D. B. Leinweber, A. I. Signal, A. G. Williams, and J. M. Zanotti , Nucl. Phys. B, Proc. Suppl. **141**, 22 (2005).

[25] F. Bissey, F. Bissey, F-G. Cao, A. R. Kitson, A. I. Signal, D. B. Leinweber, B. G. Lasscock, and A. G. Williams, Phys. Rev. D **76**, 114512 (2007).

[26] A. S. Bakry, X. Chen, and P.-M. Zhang, in *Quark Confinement and the Hadron Spectrum XI, Saint Petersburg, 2014*.

[27] A. S. Bakry, D. B. Leinweber, and A. G. Williams, AIP Conf. Proc. **1354**, 178 (2011).

[28] A. S. Bakry, D. B. Leinweber, and A. G. Williams, Phys. Rev. D **91**, 094512 (2015).

[29] O. Jahn and P. D. Forcrand, Nucl. Phys. B, Proc. Suppl. **129–130**, 700 (2004).

[30] M. Pfeuffer, G. S. Bali, and M. Panero, Phys. Rev. D **79**, 025022 (2009).

[31] N. Cardoso, M. Cardoso, and P. Bicudo, Phys. Rev. D **84**, 054508 (2011).

[32] N. Cardoso and P. Bicudo, Phys. Rev. D **87**, 034504 (2013).

[33] P. Bicudo, N. Cardoso, and M. Cardoso, Prog. Part. Nucl. Phys. **67**, 440 (2012).

[34] F. Gliozzi, Phys. Rev. D **72**, 055011 (2005).

[35] J. Kuti, *Proc. Sci.*, LAT2005 (2006) 001; JHW2005 (2006) 009 [arXiv:hep-lat/0511023].

[36] B. Silvestre-Brac, C. Semay, I. M. Narodetskii, and A. Veselov, Eur. Phys. J. C **32**, 385 (2003).

[37] P. de Forcrand and O. Jahn, Nucl. Phys. **A755**, 475 (2005).

[38] O. Andreev, Phys. Rev. D **78**, 065007 (2008).

[39] R. Sommer and J. Wosiek, Phys. Lett. **149B**, 497 (1984).
[40] H. Thacker, E. Eichten, and J. Sexton, Nucl. Phys. B, Proc. Suppl. **4**, 234 (1988).
[41] C. Alexandrou, P. de Forcrand, and O. Jahn, Nucl. Phys. B, Proc. Suppl. **119**, 667 (2003).
[42] T. T. Takahashi, H. Matsufuru, Y. Nemoto, and H. Suganuma, Phys. Rev. Lett. **86**, 18 (2001).
[43] T. T. Takahashi, H. Suganuma, Y. Nemoto, and H. Matsufuru, Phys. Rev. D **65**, 114509 (2002).
[44] H. Suganuma, S. Sasaki, and H. Toki, Nucl. Phys. **B435**, 207 (1995).
[45] H. Suganuma, H. Ichie, A. Tanaka, and K. Amemiya, Prog. Theor. Phys. Suppl. **131**, 559 (1998).
[46] H. Suganuma, K. Amemiya, A. Tanaka, and H. Ichie, Nucl. Phys. **A670**, 40 (2000).
[47] *Quantum Chromodynamics and Color Confinement*, edited by H. Suganuma, M. Fukushima, and H. Toki (World Scientific, Singapore, 2001).
[48] G. S. Bali, T. Dussel, T. Lippert, H. Neff, Z. Prkacin, and K. Schilling, Nucl. Phys. B, Proc. Suppl. **153**, 9 (2006).
[49] G. S. Bali, K. Schilling, and C. Schlichter, Phys. Rev. D **51**, 5165 (1995).
[50] K. Fabricius and O. Haan, Phys. Lett. **143B**, 459 (1984).
[51] A. D. Kennedy and B. J. Pendleton, Phys. Lett. **156B**, 393 (1985).
[52] N. Cabibbo and E. Marinari, Phys. Lett. **119B**, 387 (1982).
[53] A. S. Bakry, D. B. Leinweber, and A. G. Williams, Phys. Rev. D **85**, 034504 (2012).
[54] P. J. Moran and D. B. Leinweber, Phys. Rev. D **77**, 094501 (2008).
[55] C. Morningstar and M. Peardon, Phys. Rev. D **69**, 054501 (2004).
[56] E. V. Thuneberg, Phys. Rev. B **36**, 3583 (1987).
[57] M. G. Alford and G. Good, Phys. Rev. B **78**, 024510 (2008).
[58] K. Kasamatsu and M. Tsubota, Prog. Low Temp. Phys. **16**, 351 (2008).
[59] H. B. Nielsen and P. Olesen, Nucl. Phys. **B61**, 45 (1973).
[60] M. B. Hindmarsh and T. W. B. Kibble, Rep. Progr. Phys. **58**, 477 (1995)..
[61] J. Polchinski and A. Strominger, Phys. Rev. Lett. **67**, 1681 (1991).
[62] M. Caselle, M. Pepe, and A. Rago, J. High Energy Phys. 10 (2004) 005.
[63] A. Allais and M. Caselle, J. High Energy Phys. 01 (2009) 073.
[64] F. Gliozzi, M. Pepe, and U. J. Wiese, J. High Energy Phys. 11 (2010) 053.
[65] M. Caselle, J. High Energy Phys. 08 (2010) 063.
[66] C. Bonati, Phys. Lett. B **703**, 376 (2011).
[67] J. Kogut and L. Susskind, Phys. Rev. D **11**, 395 (1975).
[68] S. Capstick and N. Isgur, Phys. Rev. D **34**, 2809 (1986).
[69] N. Brambilla, G. M. Prosperi, and A. Vairo, Phys. Lett. B **362**, 113 (1995).
[70] M. Caselle and P. Grinza, J. High Energy Phys. 11 (2012) 174.
[71] S. O. Bilson-Thompson, D. B. Leinweber, and A. G. Williams, Ann. Phys. (N.Y.) **304**, 1 (2003).
[72] N. Brambilla, J. Ghiglieri, and A. Vairo, Phys. Rev. D **81**, 054031 (2010).
[73] N. Brambilla, F. Karbstein, and A. Vairo, Phys. Rev. D **87**, 074014 (2013).
[74] N. Cardoso, M. Cardoso, and P. Bicudo, Phys. Rev. D **88**, 054504 (2013).
[75] O. Kaczmarek, F. Karsch, E. Laermann, and M. Lutgemeier, Phys. Rev. D **62**, 034021 (2000).
[76] A. S. Bakry, D. B. Leinweber, P. J. Moran, A. Sternbeck, and A. G. Williams, Phys. Rev. D **82**, 094503 (2010).
[77] H. Suganuma, T. T. Takahashi, F. Okiharu, and H. Ichie, Nucl. Phys. B, Proc. Suppl. **141**, 92 (2005).
[78] F. Bissey, A. Signal, and D. Leinweber, Phys. Rev. D **80**, 114506 (2009).
[79] N. Cardoso and P. Bicudo, Phys. Rev. D **85**, 077501 (2012).
[80] A. S. Bakry, X. Chen, and P. Zhang, Int. J. Mod. Phys. E **23**, 1460008 (2014).